

See discussions, stats, and author profiles for this publication at: <https://www.researchgate.net/publication/264431483>

Density Differences in Embedding Theory with External Orbital Orthogonality

ARTICLE *in* THE JOURNAL OF PHYSICAL CHEMISTRY A · AUGUST 2014

Impact Factor: 2.69 · DOI: 10.1021/jp5062495 · Source: PubMed

CITATIONS

4

READS

32

3 AUTHORS, INCLUDING:



[Patrick K Tamukong](#)

North Dakota State University

3 PUBLICATIONS 10 CITATIONS

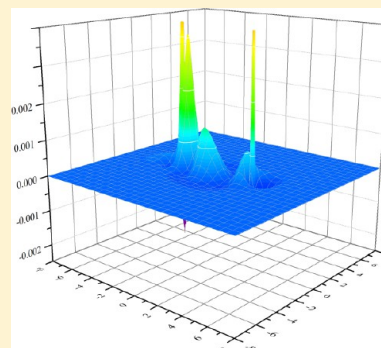
SEE PROFILE

Density Differences in Embedding Theory with External Orbital Orthogonality

Patrick K. Tamukong, Yuriy G. Khait, and Mark R. Hoffmann*

Chemistry Department, University of North Dakota, Grand Forks, North Dakota 58202-9024, United States

ABSTRACT: First results on electron densities and energies for a number of molecular complexes with different interaction strengths (ranging from ca. 0.3 to 40 kcal/mol), obtained using our recently introduced DFT-in-DFT embedding equations (i.e., Kohn–Sham equations with constrained electron density (KSCED) and external orbital orthogonality (ext orth), KSCED(x, ext orth), where x denotes the single particle support: monomer (m); supermolecular (s); or extended monomer (e)) are compared with densities from supermolecular Kohn–Sham (KS)-DFT calculations and traditional DFT-in-DFT results. Because our methodology does not rely on error-prone potentials that are not present in supermolecular KS-DFT calculations, it allows DFT-in-DFT calculations to achieve much higher accuracy than previous protocols of DFT-in-DFT that employed such potentials. It is shown that whereas conventional DFT-in-DFT embedding theory leads to errors in the electron density at the boundary between subsystems, the situation is remedied when orbital orthogonality between subsystems (i.e., external orthogonality) is enforced. Our approach reproduces KS-DFT total energies at least to the seventh decimal place (and exactly at most geometries) for the tested systems. Potential energy curves (PECs) of the separation of some of the tested systems into fragments are calculated. PECs, obtained with the new equations, using the usual Kohn–Sham equations with constrained electron density and supermolecular basis expansion [KSCED(s, ext orth, $v_T = 0$), where v_T is the nonadditive kinetic potential] were found to be virtually identical to those from conventional KS-DFT; equilibrium distances and interaction energies were reproduced to all reported digits for both local density approximation (LDA) and generalized gradient approximation (GGA) functionals. As an additional approximation, an alternative one-particle space (to the common monomer or supermolecular spaces) in which KS orbitals of a subsystem are expanded is introduced. This expansion, which we refer to as the extended monomer expansion [e.g., KSCED(e)], includes basis functions centered on atom(s) of the complementary subsystem in the interfacial region. Density differences and PECs obtained with the new equations and new one-particle space [i.e., KSCED(e, ext orth, $v_T = 0$)] were closely related to those obtained from KSCED(s, ext orth, $v_T = 0$). The new approach does not require *any* supermolecular calculations.



I. INTRODUCTION

Many ab initio methods for electronic structure calculations have applicability limited by computational costs that increase polynomially with system size. Due to this limitation, ever-expanding research efforts have considered localization (cf. refs 1–3, for example) and embedding^{4–10} techniques as a means of extending ab initio methods to the description of larger systems.

In DFT-in-DFT embedding theory,^{4–10} a system is divided into a small region of interest (the embedded subsystem, hereafter designated as A) and a larger region of secondary interest considered as the environment (hereafter, referred to as subsystem B). The environment may be further subdivided.⁸ Embedding theories seek to achieve high accuracy within a local, generally complex, embedded subsystem by describing it at a high level of approximation whereas the effect of the environment is approximated less accurately. A key bottleneck in these approaches is in the description of the often artificial boundary between subsystems. In the DFT-in-DFT embedding theory scheme, each subsystem is treated with DFT and subsystem interactions are dependent on their electron densities plus nonadditive terms resulting from the ex-

change–correlation (XC) and kinetic energy potentials. In the so-called wave function theory (WFT)-in-DFT embedding scheme,^{4,5,11} the environment subsystem is treated with DFT, generating an embedding potential that is then included as an external potential in WFT calculations on the embedded subsystem. Within DFT-in-DFT embedding theory, Wesolowski and co-workers,^{9,10} following Cortona,¹² and Senatore and Subbaswamy,¹³ partitioned the total electron density into a sum of subsystem densities,

$$\rho_{\text{tot}}(\vec{r}) = \rho_A(\vec{r}) + \rho_B(\vec{r}) \quad (1)$$

where $\rho_A(\vec{r})$ and $\rho_B(\vec{r})$ are electron densities of the respective subsystems. The total energy functional is minimized under the constraint of fixed electron number in each subsystem, but without requiring that the orbitals of a subsystem be orthogonal

Special Issue: International Conference on Theoretical and High Performance Computational Chemistry Symposium

Received: March 26, 2014

Revised: July 31, 2014

Published: August 1, 2014



to those of the complementary subsystem. Such minimization leads to a system of coupled KS-like equations for the subsystem orbitals, which are referred to as the KS equations with constrained electron density (KSCED).¹⁰ Furthermore, the orbitals of a subsystem are expanded either over basis functions centered on all nuclei of the system (termed “supermolecular basis” or KSCED(s)¹⁰) or over basis functions centered on the nuclei of the subsystem in question (termed “monomer basis” or KSCED(m)¹⁴). The energy functional of the total system is minimized by either optimizing the density of subsystem A with the fixed density of subsystem B or optimizing the densities of both subsystems iteratively to self-consistency. The former approach is termed frozen density embedding (FDE)^{9,14} and has been successfully applied to the study of weak interactions like solvent effects.^{15,16} The latter approach involves fixing (freezing) the density of one subsystem, optimizing the other and vice versa (until self-consistency is achieved) in what is often termed freeze-and-thaw cycles.¹⁰ In these optimizations, however, the final total density is not guaranteed to be the correct one. To overcome this limitation within FDE, Gritsenko and Visscher¹⁷ have recently proposed the density-orbital embedding (DOE) scheme, which affords the correct total density, $\rho_{\text{tot}}(\vec{r})$, even in regions where $\rho_{\text{B}}(\vec{r})$ may exceed $\rho_{\text{tot}}(\vec{r})$, by allowing the so-called density orbital defined for the embedded subsystem to be negative in such situations. This approach is said to broaden the range of admissible $\rho_{\text{B}}(\vec{r})$ in FDE. It remains to be shown how well this proposed scheme reproduces the total density particularly at the interface between subsystems.

Discrepancies in both the FDE and freeze-and-thaw protocols have long been attributed to inaccuracies in the nonadditive kinetic energy potential (v_{T}) that contributes to the embedding potential. Different kinetic energy functionals^{18,19} have been used for v_{T} and have yielded satisfactory results in weakly bound systems.^{19–22} These approximations, however, fail for more strongly interacting subsystems^{22–25} and can produce counterintuitive results; e.g., for all the complexes considered in ref 26, KSCED calculations using generalized gradient approximation (GGA) functionals led to worse molecular geometries than did the KSCED local density approximation (LDA), whereas conventional KS-DFT GGA calculations improved such geometries. Alternatively, Laricchia et al.^{27,28} argued that failures in the KSCED method are due to the self-interaction error (i.e., the self-energy of the electron) resulting from shortcomings in current LDA and GGA functionals and that this problem could be solved by the use of hybrid functionals. If this were indeed the case, the accuracy of embedding results should improve if the fraction of single determinant exchange were increased in the hybrid functionals. We investigated this thought within our freeze-and-thaw scheme by performing calculations on the water dimer and the $\text{Li}^+\cdots\text{Be}$ complex using the B1B95,²⁹ MPW3LYP,³⁰ and BHandHLYP³¹ hybrid functionals while varying the fraction of single determinant exchange in each case.

Efforts to improve DFT-in-DFT embedding theory are ongoing. Most focus on obtaining improved approximations to v_{T} ,²⁵ seeking an exact form of v_{T} ,³² or compensating by the introduction of a unique embedding potential, which is common to the interacting subsystems. In this regard, the emb-OEP (optimized effective potential) scheme^{6,7} was realized as well as partition DFT (PDFT).³³ Both emb-OEP and PDFT seek a unique embedding (or partition) potential

that makes subsystem densities satisfy eq 1. The emb-OEP scheme uses an extended Wu–Yang functional,^{34,35} defined as

$$W[V_{\text{emb}}] = \sum_{i=A,B} E_i[\rho_i] + \int V_{\text{emb}}(\vec{r}) \left(\sum_{i=A,B} \rho_i - \rho_{\text{ref}} \right) d\vec{r}^3 \quad (2)$$

where ρ_{ref} is the density of the total system, initially determined in a KS-DFT calculation, ρ_i are densities of subsystems, and V_{emb} is the sought embedding potential and is the Lagrange multiplier for the density constraint in eq 1. In PDFT, a partition potential similar to V_{emb} is determined iteratively.³³ Although initial tests of these techniques on small systems were appealing, they appear computationally costly (e.g., both exact embedding³² and emb-OEP^{6,7} require an initial determination of KS-orbitals and density for the total system). Production-level costs of PDFT are unknown, although pilot studies, in which the aim was only to reproduce the exact molecular density, were more expensive than conventional KS-DFT.³³

The present method has some commonality with the recently proposed “simple exact DFT embedding scheme” of Manby et al.³⁶ in that both approaches enforce intersystem or external orbital orthogonality and thereby avoid the use of kinetic energy functionals. However, our method differs epistemologically from that of Manby et al. in that their method first requires a KS-DFT calculation on the *total system*, whereas our scheme derives from traditional DFT-in-DFT embedding in which DFT calculations are only required of individual subsystems. Procedurally, Manby et al. use a level shift projection operator that shifts the energies of KS orbitals of the complementary subsystem to higher values to ensure their orthogonality to desired precision to those of the other subsystem. We include intersubsystem orbital orthogonality as an added constraint in the construction of the Lagrangian that leads to coupled Euler–Lagrange equations for the subsystems.

In the present paper, we obtain the first numerical results using our new DFT-in-DFT method that enforces orthogonality between the orbitals of the subsystems. When the orbitals of subsystems are required to be orthogonal to each other, the nonadditive kinetic energy must be exactly zero.^{14,37} Irrespective of the approximate exchange correlation (XC) functional type, the new scheme reproduces KS-DFT total energies exactly (at least to the seventh decimal place) and leads to negligible density deviations in comparison with KS-DFT densities of the tested systems. Relief and contour maps of electron density differences between DFT-in-DFT embedding, for several different options (including subsystem orthogonality), compared with KS-DFT densities for whole systems are presented. Electron density studies have previously been reported for the $\text{Li}^+\cdots\text{H}_2\text{O}$ complex,^{38,39} the hydrogen bonded complexes $\text{F}^-\cdots\text{H}_2\text{O}$,^{38,40} $\text{HF}\cdots\text{F}^-$,⁴⁰ and $\text{HF}\cdots\text{HCN}$,⁴¹ and the coordination complexes TiCl_4 and $\text{Cr}(\text{CO})_6$.²³ The deformation electron densities reported in refs 38, 39, and 41 were computed as differences between KS-DFT or KSCED(s) densities and sums of densities of isolated fragments. Kiewisch and co-workers^{23,40} also reported such deformation densities in addition to density differences between KS-DFT and KSCED(s) for the systems they studied. Here, we report density differences (designated as $\Delta\rho$) between electron densities obtained from KS-DFT and KSCED(x) (x = s (supermolecular), m (monomer), or e (extended monomer)) embedding theory for weakly bonded ($\text{CH}_4\cdots\text{CH}_4$) and hydrogen bonded ($\text{H}_2\text{O}\cdots\text{H}_2\text{O}$, $\text{H}_2\text{O}\cdots\text{F}^-$, and $\text{NH}_3\cdots\text{NH}_3$) complexes, complexes involving charge polarization ($\text{NH}_3\cdots\text{F}_2$,

$\text{Li}^+\cdots\text{H}_2\text{O}$, and $\text{C}_2\text{H}_4\cdots\text{F}_2$), and the parallel-displaced (PD) π -stacked $\text{C}_6\text{H}_6\cdots\text{C}_6\text{H}_6$ complex. The interaction energies of these systems, among others, were reported in ref 42 using both LDA (VWN5 functional of Vosko et al.⁴³ with the Thomas–Fermi⁴⁴ kinetic energy) and GGA (Perdew–Wang (PW91)^{45,46}) functionals. We have used the same functionals and geometries as used in ref 42 together with the aug-cc-pVTZ basis set in all our calculations on these systems.

The principal data of this study were electron densities, particularly when the external orthogonality constraint was enforced within KSCED(x) (x = s (supermolecular), m (monomer), or e (extended monomer), which is a new variant of one-particle space, intermediate in size between monomer and supermolecular, that is introduced herein) in comparison with KS-DFT. Calculations without enforcing orthogonality, which should be equivalent to conventional DFT-in-DFT, were done on previously studied systems partly to verify that our new program was working correctly. Full potential energy curves (PECs) for the dissociation into fragments of some of the systems we considered were computed to further investigate the performance of our new approach, KSCED(x, ext orth, $v_T = 0$), with calculations that either did not enforce orthogonality or did not enforce the vanishing of the nonadditive kinetic potential. Specifics of the calculation are included within parentheses following KSCED; an “x” = monomer (m) or supermolecular (s) or extended monomer (e) specifies the one-particle basis; “ext orth” denotes that external orthogonality was enforced; and $v_T = 0$ means that the nonadditive kinetic potential (v_T) was set to zero. In calculations where v_T is not indicated, the potential was not set to zero, e.g., KSCED(e, ext orth). Additionally, we performed calculations using hybrid functionals to investigate the effect of single determinant exchange on the accuracy of embedding energies when compared with KS-DFT.

The rest of this article is organized as follows. In section II, we begin by briefly describing DFT-in-DFT and introduce notation and then review our orthogonal orbital variant of DFT-in-DFT. In a subsequent subsection, we introduce an orbital basis that is slightly larger than the monomer basis, but substantially smaller than the supermolecular basis; we refer to this basis as extended monomer and denote it by e. A final subsection describes computational details. In section III, results of electron density differences (of above-mentioned molecular complexes) and potential energy curves (of $\text{Li}^+\cdots\text{H}_2\text{O}$, and of $\text{HF}\cdots\text{HF}$ and $\text{He}\cdots\text{Ne}$) are presented and discussed. Conclusions are given in section IV.

II. METHODOLOGY

Details of our embedding scheme have been discussed elsewhere.^{5,47} Here, we review only the key equations.

a. KS-DFT. Following Hohenberg and Kohn⁴⁸ within the constrained-search formulation,⁴⁹ the ground electronic energy of any quantum system of N electrons is obtained as the minimum of a functional of its electron density, $E_v(\rho)$,

$$E_0 = \min_{\rho \rightarrow N} E_v[\rho] \quad (3)$$

where the energy functional is defined as

$$E_v[\rho] = F[\rho] + \int v(\vec{r}) \rho(\vec{r}) d\vec{r} \quad (4)$$

$v(\vec{r})$ is the potential due to the nuclei and the functional $F[\rho]$ (involving the kinetic energy, T , and two electron interaction terms, V_{ee}) is

$$F[\rho] = \min_{\Psi \rightarrow \rho} \langle \Psi | T + V_{ee} | \Psi \rangle \quad (5)$$

The Ψ functions are normalized N -electron wave functions constrained to have electron density $\rho(\vec{r})$. The latter is itself required to meet the following constraints:

$$\int \rho(\vec{r}) d\vec{r} = N \quad \rho(\vec{r}) \geq 0 \quad \int |\nabla \rho^{1/2}|^2 d\vec{r} < \infty \quad (6)$$

The Euler form of eq 3 is

$$\frac{\delta T_s[\rho]}{\delta \rho(\vec{r})} + v_s^{\text{KS}}([\rho]; \vec{r}) = \mu_s \quad (7)$$

where the potential $v_s^{\text{KS}}([\rho]; \vec{r})$ is defined as

$$v_s^{\text{KS}}([\rho]; \vec{r}) = v(\vec{r}) + \int \frac{\rho(\vec{r}')}{|\vec{r} - \vec{r}'|} d\vec{r}' + \frac{\delta E_{xc}[\rho]}{\delta \rho(\vec{r})} \quad (8)$$

and μ_s is the Lagrange multiplier associated with the electron number conservation constraint on the density.

According to Kohn and Sham,⁵⁰ eq 7 can be written alternatively as

$$h^{\text{KS}}|\phi_m^{\text{KS}}\rangle = \epsilon_m^{\text{KS}}|\phi_m^{\text{KS}}\rangle \quad (m \in [1, N]) \quad (9)$$

where

$$h^{\text{KS}}(\vec{r}) = -\frac{1}{2}\nabla^2 + v_s^{\text{KS}}([\rho]; \vec{r}) \quad \text{and} \quad \rho(\vec{r}) = \sum_{m=1}^N |\phi_m^{\text{KS}}(\vec{r})|^2 \quad (10)$$

where $|\phi_m^{\text{KS}}\rangle$ are Kohn–Sham orbitals with corresponding eigenvalues ϵ_m^{KS} .

b. DFT-in-DFT Embedding Theory. In DFT-in-DFT embedding theory, the total density of a system is partitioned between subsystems (cf. eq 1) with fixed integer electron numbers N_A and N_B , and $\rho_A(\vec{r})$ and $\rho_B(\vec{r})$ are the corresponding densities for subsystems A and B, respectively. These densities are defined similarly to the total density (cf. eq 10, but for the respective subsystems) and are required to obey the comparable conditions of eq 6, viz.

$$\int \rho_I(\vec{r}) d\vec{r} = N_I \quad \rho_I(\vec{r}) \geq 0 \quad \int |\nabla \rho_I^{1/2}|^2 d\vec{r} < \infty \quad (I = A, B) \quad (11)$$

Analogous equations to eq 7 are defined for each subsystem

$$\frac{\delta T_s[\rho_I]}{\delta \rho_I(\vec{r})} + v_{\text{eff}}^I([\rho, \rho_I]; \vec{r}) = \mu_s^I \quad (I = A, B) \quad (12)$$

with effective potentials defined as

$$v_{\text{eff}}^I([\rho, \rho_I]; \vec{r}) = v_s^{\text{KS}}([\rho]; \vec{r}) + v_T^I([\rho, \rho_I]; \vec{r}) \quad (I = A, B) \quad (13)$$

The effective potentials differ from the KS potential, $v_s^{\text{KS}}([\rho]; \vec{r})$, by an additional term, called the nonadditive kinetic potential (v_T), defined for the respective subsystems as

$$v_T^I([\rho, \rho_I]; \vec{r}) = \frac{\delta T_s[\rho]}{\delta \rho(\vec{r})} - \frac{\delta T_s[\rho_I]}{\delta \rho_I(\vec{r})} \quad (I = A, B) \quad (14)$$

Equation 12 is solved iteratively under the assumption that the chemical potentials (i.e., Lagrange multipliers related to the electron number constraints in eq 11) with respect to the subsystems are equal ($\mu_s^A = \mu_s^B$). In thermodynamic terms, this implies that the subsystems are in equilibrium and the chemical potentials are themselves equal to that in eq 7 ($\mu_s^A = \mu_s^B = \mu_s$).

c. External Orthogonality of Orbitals. Although the electron density of a given system may be represented using essentially any set of orbitals (see, e.g., ref 51), it was shown⁴⁷ that in the particular case of DFT-in-DFT embedding theory, without a compensatory potential at the interface, the orbital sets of the subsystems must be orthogonal to each other for the total density to be expressed as a sum of fragment densities as in eq 1. Then recognizing that the densities *within* each subsystem can be obtained from an arbitrary rotation of orbitals, it is most convenient to present the external orthogonality formalism in an orthonormal basis. Let $|\bar{\phi}\rangle = |\bar{\phi}^A, \bar{\phi}^B\rangle$ be the composite orbital set within the total space ($L_{\bar{\phi}}$), where $|\bar{\phi}^A\rangle$ and $|\bar{\phi}^B\rangle$ are orthonormalized sets of orbitals of subsystems A and B, respectively. Then one can construct an orthonormal orbital set within $L_{\bar{\phi}}$ as $|\bar{\phi}^{\text{orth}}\rangle = |\bar{\phi}\rangle S^{-1/2}$, where S is the full overlap matrix

$$S = \langle \bar{\phi} | \bar{\phi} \rangle = \begin{pmatrix} \mathbf{I}_{AA} & \mathbf{S}_{AB} \\ \mathbf{S}_{BA} & \mathbf{I}_{BB} \end{pmatrix} \quad (15)$$

Because $|\bar{\phi}^A\rangle$ and $|\bar{\phi}^B\rangle$ are orthonormalized orbitals sets, the densities of the respective subsystems can be expressed in diagonal quadratic form as

$$\rho_A(\mathbf{r}) = \sum_{a=1}^{N_A} |\phi_a^A(\mathbf{r})|^2 \quad \rho_B(\mathbf{r}) = \sum_{b=1}^{N_B} |\phi_b^B(\mathbf{r})|^2 \quad (16)$$

where N_A and N_B are integer numbers of electrons in subsystems A and B, respectively. In terms of the orthonormal set $|\bar{\phi}^{\text{orth}}\rangle = |\bar{\phi}\rangle S^{-1/2}$, the total density can then be expressed as

$$\begin{aligned} \rho_A(\mathbf{r}) + \rho_B(\mathbf{r}) &= \sum_{k,l=1}^N \phi_k^{\text{orth}}(\mathbf{r}) S_{kl} \phi_l^{\text{orth}*}(\mathbf{r}) \\ &= \sum_{k=1}^N |\phi_k^{\text{orth}}(\mathbf{r})|^2 + \sum_{k,l=1}^N \phi_k^{\text{orth}}(\mathbf{r}) (\mathbf{S} - \mathbf{I})_{kl} \phi_l^{\text{orth}*}(\mathbf{r}) \end{aligned} \quad (17)$$

Thus, for given sets of orbitals, $|\bar{\phi}^A\rangle$ and $|\bar{\phi}^B\rangle$, the sum $\rho_A(\mathbf{r}) + \rho_B(\mathbf{r})$ can be represented in block diagonal quadratic form only if $\mathbf{S}_{AB} = \mathbf{S}_{BA} = 0$.

The following Lagrangian is constructed with this additional constraint of external orbital orthogonality included⁴⁷

$$\begin{aligned} \Omega[\bar{\phi}^A, \bar{\phi}^B] &= E^S[\bar{\phi}^A, \bar{\phi}^B] - \sum_{I=A,B} \sum_{c,c'=1}^{N_I} \Theta_{cc'}^I \langle \phi_c^I | \phi_{c'}^I \rangle \\ &\quad - \sum_{a=1}^{N_A} \sum_{b=1}^{N_B} \alpha_{ba} \langle \phi_a^A | \phi_b^B \rangle - \sum_{a=1}^{N_A} \sum_{b=1}^{N_B} \beta_{ab} \langle \phi_b^B | \phi_a^A \rangle \end{aligned} \quad (18)$$

The first term on the right-hand side of eq 18 is the energy functional for the total system expressed as a functional of the subsystem orbital sets, the second term is related to the number conservation constraint in eq 11, and the last two terms express the constraint of intersystem orbital orthogonality. It is assumed that the subsystem orbitals can be expressed in terms of a supermolecular basis, so that all multiplications in eq 18 are commensurate; in the subsequent subsection, it will be

shown that the number of nonzero contributions can be limited. It should also be realized that the v_T (cf. eq 14) in the energy functional, E^S , vanishes for orthogonal subset orbitals;^{14,37} it is retained to facilitate numerical evaluation of its effect. $\Theta_{cc'}$, α_{ba} , and β_{ab} are Lagrange multipliers associated with the constraints. Physically, $\langle \phi_a^A | \phi_b^B \rangle$ (or $\langle \phi_b^B | \phi_a^A \rangle$) represent the subspace of projected orbitals of subsystem B onto subsystem A (or of A onto B). The Lagrange multipliers ensure that the projections equal zero in the case of external orthogonality. Minimization of the defined Lagrangian with respect to variations in $\langle \phi_a^A |$ results in a generalized KS equation⁵² for the subsystem

$$\begin{aligned} [h^{\text{KS}} + v_T^A] |\phi_a^A\rangle &= \sum_{a'}^{N_A} |\phi_{a'}^A\rangle \Theta_{a'a}^A + \sum_{b=1}^{N_B} |\phi_b^B\rangle \alpha_{ba} \\ (a \in [1, N_A]) \end{aligned} \quad (19)$$

Because the total energy is invariant with respect to unitary orbital transformations within subsystems, we consider canonical orbitals to constitute the set $\bar{\phi}^A$ (for which $\Theta_{aa'}^A = \delta_{aa'} \epsilon_a^A$) and recast eq 19 as

$$\begin{aligned} [h^{\text{KS}} + v_T^A] |\phi_a^A\rangle &= |\phi_a^A\rangle \epsilon_a^A + \sum_{b=1}^{N_B} |\phi_b^B\rangle \alpha_{ba} \\ (a \in [1, N_A]) \end{aligned} \quad (20)$$

Left projecting against orbitals in the B subsystem obtains

$$\alpha_{ab} = \alpha_{ba} = \langle \phi_b^B | h^{\text{KS}} + v_T^A | \phi_a^A \rangle \quad (21)$$

considering external orthogonality (i.e., $\langle \phi_b^B | \phi_a^A \rangle = 0$). Substituting eq 21 into eq 20 and rearranging leads to

$$(I - P^B)[h^{\text{KS}} + v_T^A] |\phi_a^A\rangle = |\phi_a^A\rangle \epsilon_a^A \quad (22)$$

Similar arguments lead to

$$(I - P^A)[h^{\text{KS}} + v_T^B] |\phi_b^B\rangle = |\phi_b^B\rangle \epsilon_b^B \quad (23)$$

for the complementary subsystem B where v_T^A and v_T^B are defined in eq 14 and $P^B = |\bar{\phi}^B\rangle \langle \bar{\phi}^B| = \sum_{b=1}^{N_B} |\bar{\phi}_b^B\rangle \langle \bar{\phi}_b^B|$ is the projector on the KS orbitals of subsystem B (P^A is defined similarly). Unfortunately, the modified one-electron Hamiltonian (i.e., Fockian), $(I - P^B)[h^{\text{KS}} + v_T^A]$ (or $(I - P^A)[h^{\text{KS}} + v_T^B]$), is asymmetric. However, transforming it to symmetric form is straightforward and accomplished by first noting that under the external orthogonality constraint, $(I - P^B)|\bar{\phi}^A\rangle = |\bar{\phi}^A\rangle$ and $(I - P^A)|\bar{\phi}^B\rangle = |\bar{\phi}^B\rangle$. Thus, eqs 22 and 23 can be recast as

$$(I - P^B)[h^{\text{KS}} + v_T^A](I - P^B) |\phi_a^A\rangle = |\phi_a^A\rangle \epsilon_a^A \quad (24a)$$

$$(I - P^A)[h^{\text{KS}} + v_T^B](I - P^A) |\phi_b^B\rangle = |\phi_b^B\rangle \epsilon_b^B \quad (24b)$$

In eq 22, 23 and 24, I is used to represent the identity operator within the total one-electron space and can be written in terms of atomic orbitals as

$$I = I_T = |\bar{\chi}_T\rangle S_{TT}^{-1} \langle \bar{\chi}_T| \quad (I_T)^2 = I_T \quad (25)$$

where $\bar{\chi}_T$ is a set of atomic basis functions with overlap matrix $S_{TT} = \langle \bar{\chi}_T | \bar{\chi}_T \rangle$.

d. Monomer and Extended Monomer Basis Expansions. In practice, it is computationally more costly to perform embedding calculations with supermolecular basis set expansions (KSCED(s)) than with conventional KS-DFT on the total system. A good embedding scheme should provide an

advantageous cost to accuracy ratio. Unfortunately, use of monomer basis expansions (KSCED(m)), except for cases of very weakly interacting systems, often lead to notably less accurate results than those from KSCED(s). Thus, we introduce what we term “extended monomer basis expansions”, denoted by KSCED(e), where the KS orbitals of each subsystem are expanded not only over atomic basis functions centered on atoms of the subsystem but also over atomic functions centered on atoms in the complementary subsystem close to the boundary or interfacial region. To clarify this, consider the pictorial representation in Figure 1.

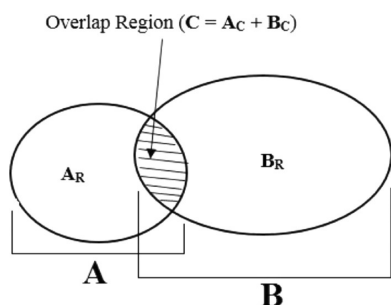


Figure 1. Schematic diagram illustrating extended monomer bases.

Suppose that nuclei of subsystem A are described as $A = A_R + A_C$ and those of subsystem B as $B = B_C + B_R$, where $C = A_C + B_C$ represents nuclei within the overlap region between A and B whose atomic basis functions are used in the expansion of orbitals of both subsystems. Atomic functions in the supermolecular basis set can be ordered as

$$|\bar{\chi}_T\rangle = |\bar{\chi}_{A_R}, \bar{\chi}_{A_C}, \bar{\chi}_{B_C}, \bar{\chi}_{B_R}\rangle = |\bar{\chi}_{A_R}, \bar{\chi}_C, \bar{\chi}_{B_R}\rangle \quad (26)$$

whereas those in the subsystem-specific “extended monomer” basis sets are described as

$$|\bar{\chi}_A\rangle = |\bar{\chi}_{A_R}, \bar{\chi}_C\rangle \quad |\bar{\chi}_B\rangle = |\bar{\chi}_C, \bar{\chi}_{B_R}\rangle \quad (27)$$

where $|\bar{\chi}_C\rangle = |\bar{\chi}_{A_C}, \bar{\chi}_{B_C}\rangle$ is the set of atomic orbitals centered on all nuclei of the overlap region. KS orbitals of the subsystems are expanded over these bases. We emphasize here that partitioning of a system is flexible and arbitrary, although some choices are sure to be more advantageous than others. Once a choice of regions is made, the selection of overlap region becomes one of desired accuracy. Whereas eq 24 is suitable for KSCED(s) calculations, in the case of KSCED(m) and KSCED(e) calculations, additional modifications must be made because, for such cases, the KS orbitals, $\bar{\phi}^A$ and $\bar{\phi}^B$, belong to different (overlapping) subspaces. For such situations, let us define the operators

$$I_A = |\bar{\chi}_A\rangle S_{AA}^{-1} \langle \bar{\chi}_A| \quad I_A |\bar{\chi}_A\rangle = |\bar{\chi}_A\rangle \quad (28a)$$

$$I_B = |\bar{\chi}_B\rangle S_{BB}^{-1} \langle \bar{\chi}_B| \quad I_B |\bar{\chi}_B\rangle = |\bar{\chi}_B\rangle \quad (28b)$$

where $S_{AA} = \langle \bar{\chi}_A | \bar{\chi}_A \rangle$ and $S_{BB} = \langle \bar{\chi}_B | \bar{\chi}_B \rangle$ are overlap matrices associated with $\bar{\chi}_A$ and $\bar{\chi}_B$. Because $I_A |\bar{\phi}^A\rangle = |\bar{\phi}^A\rangle$ and $I_B |\bar{\phi}^B\rangle = |\bar{\phi}^B\rangle$, eqs 22 and 23 can be recast as

$$I_A (I - P^B) I_T h^A I_A |\bar{\phi}^A\rangle = |\bar{\phi}^A\rangle \epsilon^A \quad (29a)$$

$$I_B (I - P^A) I_T h^B I_B |\bar{\phi}^B\rangle = |\bar{\phi}^B\rangle \epsilon^B \quad (29b)$$

where the identity operator I_T was defined in eq 25. To ensure the orthogonality of $\bar{\phi}^A$ to $\bar{\phi}^B$, it suffices to consider, within the subspace of projected orbitals $I_A |\bar{\phi}^B\rangle$, only such linear combinations,

$$|\bar{\phi}^B\rangle = I_A |\bar{\phi}^B\rangle = |\tilde{\phi}_1^B, \tilde{\phi}_2^B, \dots, \tilde{\phi}_{\tilde{N}_B}^B\rangle \quad (30)$$

that have nonzero projections on $L_A = \text{Span}\{\bar{\chi}_A\}$. The number of such vectors will equal the number, \tilde{N}_B , of nonzero eigenvalues ($0 \leq \tilde{N}_B \leq N_B$) of the matrix $\langle \bar{\phi}^B | I_A | \bar{\phi}^B \rangle$.

The orthonormal set $\tilde{\phi}^B$ is obtained by diagonalizing the matrix $\langle \bar{\phi}^B | I_A | \bar{\phi}^B \rangle$ and selecting the \tilde{N}_B eigenvectors ($0 \leq \tilde{N}_B \leq N_B$) with nonzero eigenvalues. If $V_{N_B \tilde{N}_B}^B$ is the matrix of the \tilde{N}_B eigenvectors and $\mathbf{d}_{N_B}^B = \text{diag}\{d_1^B, \dots, d_{\tilde{N}_B}^B\}$ is the diagonal matrix of corresponding eigenvalues, then the set $\tilde{\phi}^B$ can be written as

$$|\tilde{\phi}^B\rangle = I_A |\bar{\phi}^B\rangle V_{N_B \tilde{N}_B}^B (\mathbf{d}_{N_B}^B)^{-1/2} = |\bar{\chi}_A\rangle U_{N_B}^B$$

$$\langle \tilde{\phi}^B | \tilde{\phi}^B \rangle = I_{\tilde{N}_B \tilde{N}_B} \quad (31)$$

where $I_{N_B \tilde{N}_B}$ is the identity matrix within the subspace of the \tilde{N}_B vectors, $\tilde{\phi}^B$, and

$$U_{A N_B}^B = S_{AA}^{-1} \langle \bar{\chi}_A | \tilde{\phi}^B \rangle$$

$$= S_{AA}^{-1} \langle \bar{\chi}_A | \bar{\phi}^B \rangle V_{N_B \tilde{N}_B}^B (\mathbf{d}_{N_B}^B)^{-1/2}$$

$$= S_{AA}^{-1} S_{AB} C_{B N_B}^B V_{N_B \tilde{N}_B}^B (\mathbf{d}_{N_B}^B)^{-1/2} \quad (32)$$

determines the expansion of the vectors $\tilde{\phi}^B$ within $L_A = \text{Span}\{\bar{\chi}_A\}$. As a result, the projector P^B (cf. eq 29a) can be replaced with

$$P^{\tilde{\phi}^B} = I_A P^{\tilde{\phi}^B} I_A = I_A |\tilde{\phi}^B\rangle \langle \tilde{\phi}^B | I_A \quad (33)$$

Similar equations can be written for subsystem A. In the limiting case of the supermolecular basis, where $\bar{\chi}_A \rightarrow \bar{\chi}_T$ and $\bar{\chi}_B \rightarrow \bar{\chi}_T$, one has $P^{\tilde{\phi}^A} \rightarrow P^A$ (because $|\tilde{\phi}^A\rangle \rightarrow |\bar{\phi}^A\rangle$) and likewise $P^{\tilde{\phi}^B} \rightarrow P^B$. It is not difficult to verify that the new projectors $P^{\tilde{\phi}^A}$ and $P^{\tilde{\phi}^B}$ satisfy the conditions $|\bar{\phi}^A\rangle = (I_A - P^{\tilde{\phi}^B}) |\bar{\phi}^A\rangle$ and $|\bar{\phi}^B\rangle = (I_B - P^{\tilde{\phi}^A}) |\bar{\phi}^B\rangle$. Thus, the asymmetric eqs 29a and 29b can be recast in Hermitian form as

$$(I_A - P^{\tilde{\phi}^B}) I_A h^A I_A (I_A - P^{\tilde{\phi}^B}) |\bar{\phi}^A\rangle = |\bar{\phi}^A\rangle \epsilon^A \quad (34a)$$

$$(I_B - P^{\tilde{\phi}^A}) I_B h^B I_B (I_B - P^{\tilde{\phi}^A}) |\bar{\phi}^B\rangle = |\bar{\phi}^B\rangle \epsilon^B \quad (34b)$$

which are our final working equations for the extended monomer basis.

e. Computational Details. KSCED calculations with supermolecular, our new extended monomer, and monomer basis expansions, KSCED(s), KSCED(e), and KSCED(m) respectively, were performed using locally developed computer programs based on methods briefly described above. As noted above, the designations KSCED(x, ext orth) and KSCED(x, ext orth, $\nu_T = 0$) are used to specify calculations that included external orthogonality, with and without setting the nonadditive kinetic potential (ν_T) to zero. Electron densities were computed using a locally developed code. Relief and contour maps of

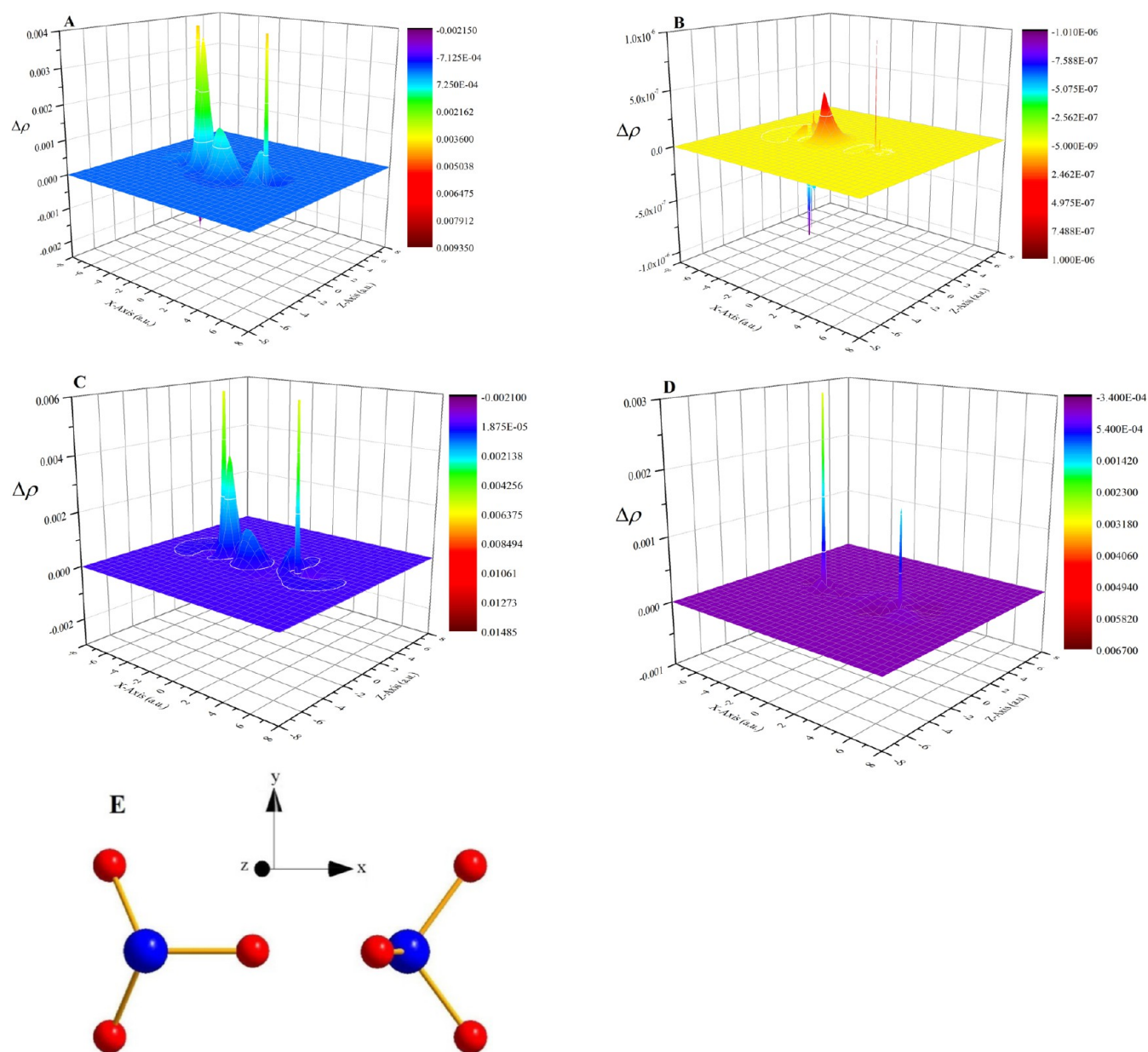


Figure 2. Density difference relief maps (xz -plane) for the $\text{NH}_3 \cdots \text{NH}_3$ complex, positioned as shown. The maps display the density differences: A = KS-DFT – KSCED(s); B = KS-DFT – KSCED(s, ext orth, $\nu_T = 0$); C = KS-DFT – KSCED(e); D = KS-DFT – KSCED(e, ext orth, $\nu_T = 0$). Image E is the geometry of the complex.

electron density differences ($\Delta\rho$), relative to conventional KS-DFT calculations, were obtained for the weakly bonded $\text{CH}_4 \cdots \text{CH}_4$ complex, hydrogen bonded complexes ($\text{H}_2\text{O} \cdots \text{H}_2\text{O}$, $\text{H}_2\text{O} \cdots \text{F}^-$, and $\text{NH}_3 \cdots \text{NH}_3$), complexes involving charge polarization ($\text{Li}^+ \cdots \text{H}_2\text{O}$, $\text{NH}_3 \cdots \text{F}_2$, and $\text{C}_2\text{H}_4 \cdots \text{F}_2$), and the parallel-displaced (PD) π -stacked $\text{C}_6\text{H}_6 \cdots \text{C}_6\text{H}_6$ complex. All (except $\text{H}_2\text{O} \cdots \text{F}^-$ and $\text{Li}^+ \cdots \text{H}_2\text{O}$) were computed at the same optimized geometries of Zhao and Truhlar,⁵³ which were previously used by Dulak and Wesolowski⁴² to determine interaction energies of these complexes using the VWN⁴³ and PW91^{45,45} functionals with the aug-cc-pVTZ⁵⁴ and MG3S⁵⁵ basis sets. We also used the VWN5 and PW91 functionals for all complexes in this study and the aug-cc-pVTZ basis set, except for the $\text{H}_2\text{O} \cdots \text{F}^-$ complex where we used the VWN⁴³ functional and the aug-cc-pVQZ⁵⁶ basis set and the $\text{Li}^+ \cdots \text{H}_2\text{O}$ complex where the cc-pVDZ⁵⁶ basis set was used with VWN

and PW91 functionals. All densities were obtained on a cubic grid with a step size of 0.01 bohr. (N.B. Of course, the maps only show electron density differences for chosen planes through the complexes.) For each given spatial grid point, the density was the sum of contributions from the fragments in embedding calculations. The density difference maps were obtained using OriginPro 8.6 64Bit⁵⁷ whereas graphical representations of molecular structures were generated from Diamond (version 3).⁵⁸ We computed density differences as $\Delta\rho = (\text{electron density from KS-DFT calculation on total system}) - \text{KSCED}(x)$ [or $\text{KSCED}(x, \text{ext orth})$ or $\text{KSCED}(x, \text{ext orth } \nu_T = 0)$] density. For density differences of the $\text{H}_2\text{O} \cdots \text{F}^-$ and $\text{Li}^+ \cdots \text{H}_2\text{O}$ complexes, we additionally used the designations $\Delta\rho^m$, where m represents KS or KSCED(m), to denote definitions of $\Delta\rho$ similar to those used in ref 39 [i.e., density difference = (density of KS-DFT or KSCED(m)) –

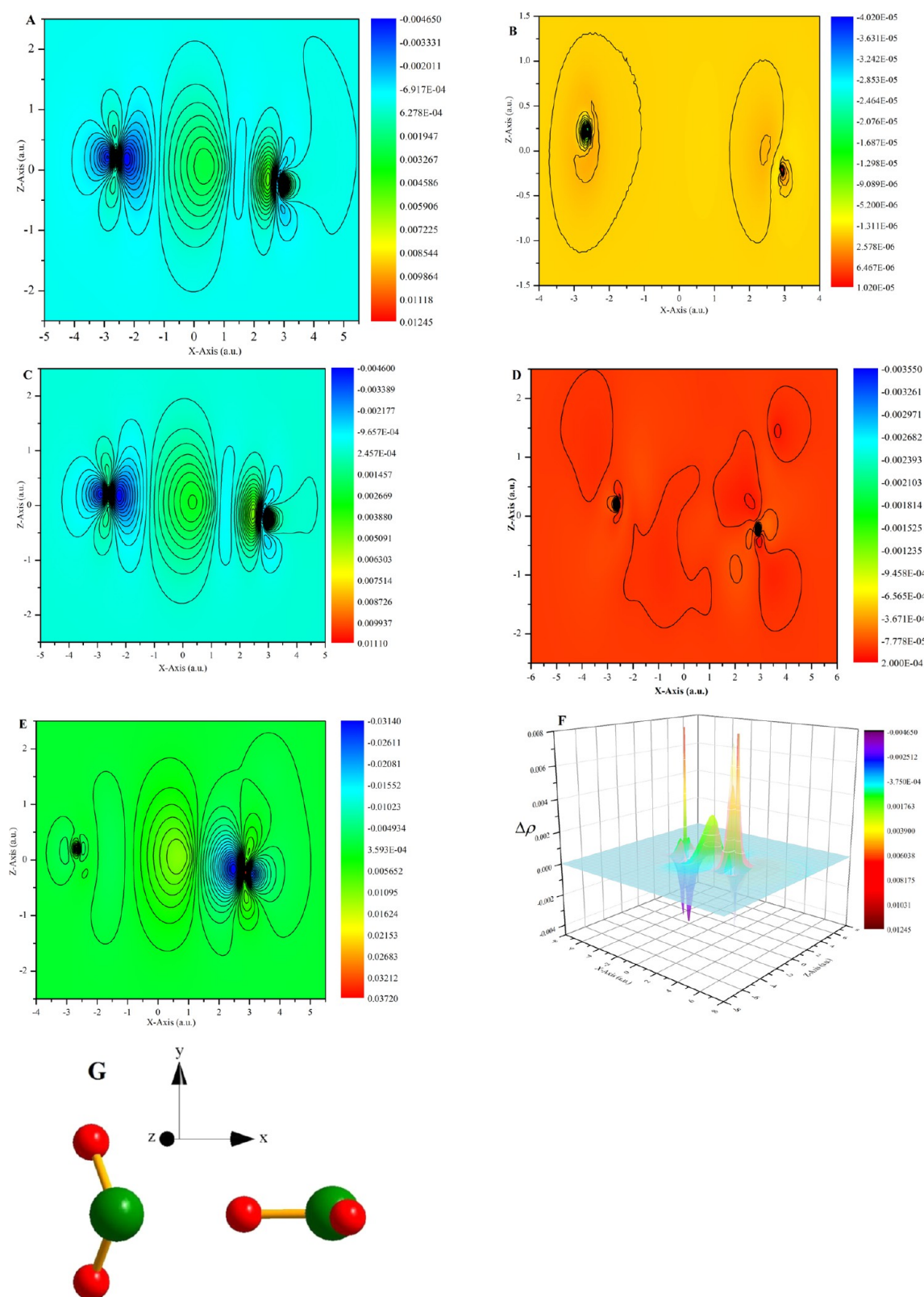


Figure 3. Density difference relief and contour maps (xz -plane) for the $\text{H}_2\text{O} \cdots \text{H}_2\text{O}$ complex, positioned as shown. The maps display the density differences: A = KS-DFT – KSCED(s); B = KS-DFT – KSCED(s, ext orth, $\nu_T = 0$); C = KS-DFT – KSCED(e); D = KS-DFT – KSCED(e, ext orth, $\nu_T = 0$); E = KS-DFT – KSCED(s, ext orth); F = superposition of (KS-DFT – KSCED(s)) surfaces from VWN5 and PW91 calculations, where the surface with rainbow color palette is that from VWN5. Image G is the geometry of the complex.

(sum of densities of isolated fragments computed using KS method)]. Program specifications were set as follows: integration threshold = 5.749×10^{-11} ; self-consistent field

energy convergence criterion = 10^{-6} ; maximum number of freeze-and-thaw cycles (e.g., macroiterations) = 20; gradient convergence criterion = 10^{-8} ; overlapping degeneracy criterion

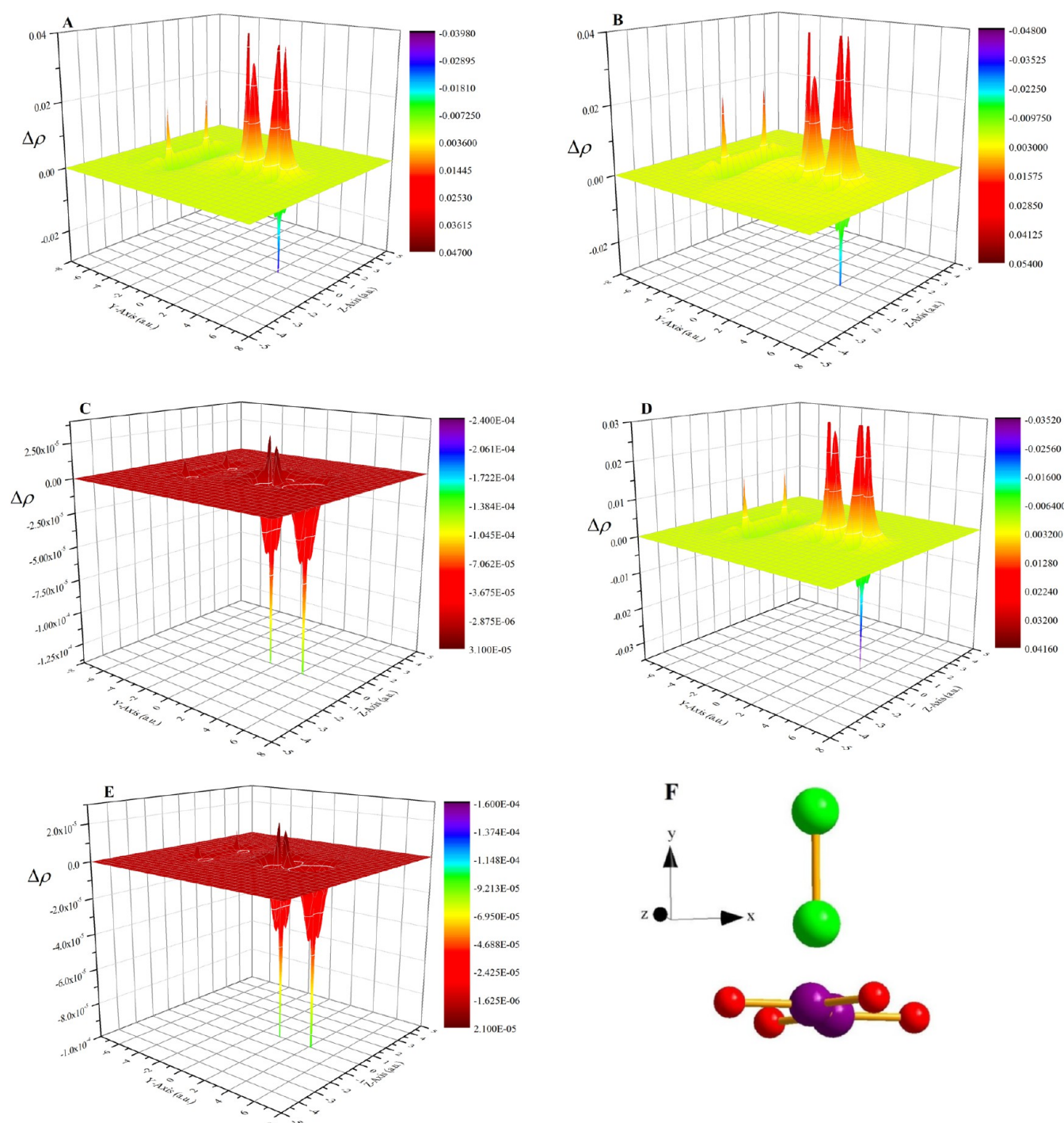


Figure 4. Density difference relief maps (yz -plane) for the $F_2 \cdots C_2H_4$ complex, positioned as shown. The maps display the density differences: A = KS-DFT – KSCED(s); B = KS-DFT – KSCED(s, ext orth); C = KS-DFT – KSCED(s, ext orth, $\nu_T = 0$); D = KS-DFT – KSCED(s); E = KS-DFT – KSCED(s, ext orth, $\nu_T = 0$). Images A–C are based on the VWN5 functional, whereas D and E used PW91. Image F is the geometry of the complex.

$= 2.22 \times 10^{-15}$; a Mura–Knowles log3 grid type⁵⁹ with 96 radial and 302 angular grid points was used. Potential energy curves (PECs) for the separation of $HF \cdots HF$ into HF molecular fragments (computed using aug-cc-pVTZ⁵⁴ with VWN5⁴³ and PW91^{45,45}), the separation of $Li^+ \cdots H_2O$ into Li^+ and H_2O (computed using cc-pVDZ⁵⁶ with VWN⁴³ and PW91,^{45,45} and of the separation of $He \cdots Ne$ into atoms (computed with VWN and aug-cc-pVTZ) were also obtained. These are used to further assess the performance of KSCED(s,

ext orth, $\nu_T = 0$) and KSCED(e, ext orth, $\nu_T = 0$) methods in comparison with KSCED(m), KSCED(e), KSCED(s), and KS-DFT. Lastly, we performed calculations on the water dimer (at the geometry of Zhao and Truhlar,⁵³) using the B1B95,²⁹ MPW3LYP,³⁰ and BHandHLYP³¹ hybrid functionals (and also on the $Li^+ \cdots Be$ complex at 2.6 Å using B3LYP^{60–62}) while varying the fraction of single determinant exchange to investigate the effect of exact exchange on the discrepancy in the embedding energy relative to KS-DFT. Where evaluated,

the nonadditive kinetic potential was determined by the Thomas–Fermi (TF) approximation⁴⁴ to the kinetic energy functional (with LDA functionals) or the Lembarki–Chermette¹⁸ kinetic energy functional (LC94) with the GGA functional (PW91) and the MPW3LYP hybrid functional. The B3LYP, BHandHLYP, and B1B95 hybrid functionals included the LLP kinetic energy functional.⁶³

III. RESULTS AND DISCUSSION

a. Electron Density Differences. Electron density difference relief and contour maps are shown in Figures 2–9 for all systems included in this study. For each system, density differences on the plane that has the highest number of atoms, and hence highest electron density, in the system are shown. All density difference values are reported in electrons per cubic bohr (e/a_0^3).

i. $\text{NH}_3 \cdots \text{NH}_3$. The $\Delta\rho$ relief maps for $\text{NH}_3 \cdots \text{NH}_3$ are shown in Figure 2, obtained using the PW91 functional. The maps are labeled A to D and represent the density differences: A = KS-DFT – KSCED(s); B = KS-DFT – KSCED(s, ext orth, $\nu_T = 0$); C = KS-DFT – KSCED(e); D = KS-DFT – KSCED(e, ext orth, $\nu_T = 0$). Image E is the geometry of the complex. Each NH_3 molecule was treated as a subsystem in KSCED(x) or KSCED(x, ext orth, $\nu_T = 0$) calculations. The density difference in the xz -plane is shown. As can be seen in images A and C, there is accumulation of electron density in the interfacial region between subsystems and a distortion of subsystem densities. The topologies of A and C are quite similar and show density deviations on the order of $10^{-2} e/a_0^3$. This indicates that the extended monomer basis is a good approximation to the supermolecular basis expansion. When the external orthogonality constraint is enforced, density deviations become negligible, decreasing to on the order of $10^{-7} e/a_0^3$ in the case of KSCED(s, ext orth, $\nu_T = 0$) calculations (image B) and $10^{-4} e/a_0^3$ in the case of KSCED(e, ext orth, $\nu_T = 0$) calculations (image D). Comparing A and C with B and D shows that accounting for external orthogonality improves the agreement of embedding densities with whole system KS-DFT calculations. Similar plots (not shown) were obtained with the VWN5 functional and found to be similar to those presented here for the PW91 functional. The interaction energy of $\text{NH}_3 \cdots \text{NH}_3$ was computed in ref 42 to be 3.74 kcal/mol from KSCED(s) using VWN5 and 4.26 kcal/mol using PW91. We obtained 3.71 kcal/mol (with VWN5) and 4.24 kcal/mol (with PW91) using our computer programs for KSCED(s). The newly developed embedding method, KSCED(s, ext orth, $\nu_T = 0$), and KS-DFT results (i.e., 5.15 kcal/mol with VWN5 versus 3.34 kcal/mol with PW91) agreed to within 0.01 kcal/mol. In KSCED(e) calculations, in which the basis functions of the N atom and one H atom of the complementary subsystem were additionally used in expanding KS orbitals of each system, 3.70 kcal/mol (with VWN5) and 4.22 kcal/mol (with PW91) were obtained, whereas KSCED(e, ext orth, $\nu_T = 0$) calculations predicted an interaction energy that was lower than KS-DFT by only 0.066 kcal/mol (VWN5; 0.068 kcal/mol with PW91). By accounting for external orbital orthogonality and setting the nonadditive kinetic potential (cf. eq 14) to its theoretical value of zero, we reproduced the KS-DFT interaction energies to within 0.01 kcal/mol in KSCED(s, ext orth, $\nu_T = 0$) and nearly as well as when the much smaller, new “extended monomer” was used.

ii. $\text{H}_2\text{O} \cdots \text{H}_2\text{O}$. Isocontour and relief density difference maps for $\text{H}_2\text{O} \cdots \text{H}_2\text{O}$, obtained using the VWN5 functional, are

shown in Figure 3. The maps, labeled A through E, represent density differences: A = KS-DFT – KSCED(s); B = KS-DFT – KSCED(s, ext orth, $\nu_T = 0$); C = KS-DFT – KSCED(e); D = KS-DFT – KSCED(e, ext orth, $\nu_T = 0$); E = KS-DFT – KSCED(s, ext orth). Map F is a superposition of KS-DFT – KSCED(s) surfaces from VWN5 and PW91 calculations, where the surface with the rainbow color palette is that from VWN5, whereas image G specifies the geometry of the complex. Each H_2O molecule was treated as a subsystem in KSCED(x), KSCED(x, ext orth), or KSCED(x, ext orth, $\nu_T = 0$) calculations. The density difference in the xz -plane is again shown. Isocontours in A are shown in the range $[-0.00465, +0.01245]$ in steps of $4.275 \times 10^{-4} e/a_0^3$, in C in the range $[-0.0046, +0.0111]$ in steps of $3.925 \times 10^{-4} e/a_0^3$, and in E in the range $[-0.0314, +0.0372]$ in steps of $1.715 \times 10^{-3} e/a_0^3$. As can be seen in images A and C, there is a buildup of electron density at the intermolecular region. Inclusion of the ext orth constraint without zeroing the nonadditive kinetic potential (ν_T) in supermolecular basis calculations [KSCED(s, ext orth)] fails to improve the density (image E). However, by setting ν_T to zero, density deviations become negligible, decreasing to on the order of $10^{-6} e/a_0^3$ in the case of KSCED(s, ext orth, $\nu_T = 0$) calculations (image B) and $10^{-4} e/a_0^3$ in the case of KSCED(e, ext orth, $\nu_T = 0$) calculations (image D). As can be seen in image F, the two surfaces are quite similar, with the PW91 surface lying slightly above the VWN5 surface at most points except for the intermolecular region. The interaction energy computed in ref 42 for this system was 4.92 kcal/mol using VWN5 in KSCED(s). We obtained 4.90 kcal/mol in KSCED(s) calculations using VWN5. Meanwhile, KSCED(s, ext orth, $\nu_T = 0$) calculations using VWN5 reproduced the KS-DFT interaction energy of 7.29 kcal/mol exactly (i.e., to the fifth decimal place) whereas KSCED(e, ext orth, $\nu_T = 0$) calculations predicted an interaction energy that was only 0.045 kcal/mol less than the KS-DFT value.

iii. $\text{F}_2 \cdots \text{C}_2\text{H}_4$. The $\Delta\rho$ relief maps, obtained with VWN5 and PW91 functionals, for $\text{F}_2 \cdots \text{C}_2\text{H}_4$ are shown in Figure 4. The maps are labeled A to E and represent the density differences: A = KS-DFT – KSCED(s); B = KS-DFT – KSCED(s, ext orth); C = KS-DFT – KSCED(s, ext orth, $\nu_T = 0$); D = KS-DFT – KSCED(s); and E = KS-DFT – KSCED(s, ext orth, $\nu_T = 0$). Images A to C are from VWN5 whereas D and E are from PW91 calculations. Image F specifies the geometry of the complex. The density difference in the yz -plane is shown. As shown in images A, B, and D, there is net density buildup within F_2 and depletion within C_2H_4 . In other words, the density of F_2 is underestimated and that of C_2H_4 is overestimated in KSCED calculations. However, enforcing external orbital orthogonality and zeroing the nonadditive kinetic potential renders density deviations negligibly small (of the order of $10^{-5} e/a_0^3$ with both VWN5 (image C) and PW91 (image E) functionals). Because the total number of electrons in each subsystem is fixed in embedding calculations (cf. eqs 16), this study demonstrates that charge polarization within each subsystem is calculated correctly. Images A, B, and C show that buildup of electron density is minimal in the interfacial region between the fragments. This is not surprising given that a reference binding energy of only 1.06 kcal/mol was reported in ref 42 for this system, which is particularly small. The ref 42 study predicted that $\text{F}_2 \cdots \text{C}_2\text{H}_4$ was unbound with VWN5 and had a binding energy of 0.76 kcal/mol with PW91 in KSCED(m) calculations. We obtained 0.10 kcal/mol (with VWN5) and 0.76 kcal/mol (with PW91) using KSCED(m).

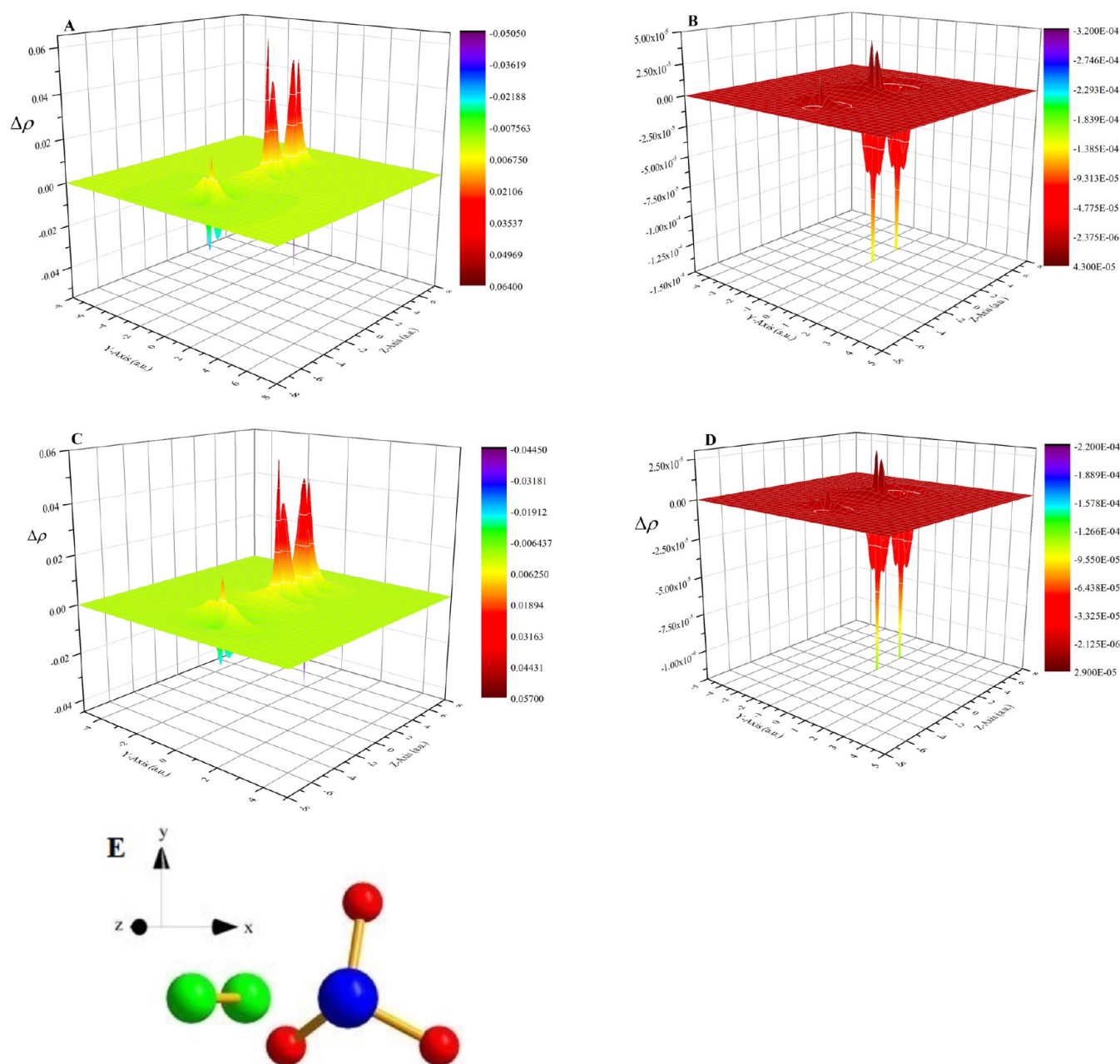


Figure 5. Density difference relief maps (yz -plane) for the $F_2 \cdots NH_3$ complex, positioned as shown. The maps display the density differences: A = KS-DFT – KSCED(s); B = KS-DFT – KSCED(s, ext orth, $\nu_T = 0$); C = KS-DFT – KSCED(s); D = KS-DFT – KSCED(s, ext orth, $\nu_T = 0$). Images A and B are based on the VWN5, whereas C and D used PW91. Image E is the geometry of the complex.

On the other hand, KSCED(s, ext orth, $\nu_T = 0$) calculations using VWN5 reproduced the KS-DFT interaction energy (of 1.06 kcal/mol) to within 0.01 kcal/mol, whereas KSCED(s) gave an interaction energy of only 0.33 kcal/mol.

iv. $F_2 \cdots NH_3$. The $\Delta\rho$ relief maps for $F_2 \cdots NH_3$ are shown in Figure 5, obtained with VWN5 and PW91 functionals. The maps are labeled A to D and represent the density differences: A = KS-DFT – KSCED(s); B = KS-DFT – KSCED(s, ext orth, $\nu_T = 0$); C = KS-DFT – KSCED(s); D = KS-DFT – KSCED(s, ext orth, $\nu_T = 0$). Images A and B are from calculations using the VWN5 functional whereas C and D are from PW91 calculations. Image E specifies the geometry of the complex. The $\Delta\rho$ values on the yz -plane are shown. Just as for $F_2 \cdots C_2H_4$, the main distortions in electron density are within the F_2 and NH_3 molecules (images A and C), with the density

of F_2 underestimated in KSCED(s) calculations relative to KS-DFT and that of NH_3 overestimated. There is minimal buildup of electron density difference at the interfacial region. Again, it is seen that accounting for external orthogonality and setting the nonadditive kinetic potential to its theoretical value of zero enables embedding theory densities to represent whole molecule KS-DFT calculations well; density deviations are diminished from on the order of 10^{-2} to 10^{-6} e/a_0^3 for both VWN5 (image B) and PW91 (image D) functionals. The interaction energy for this system was found in ref 42 to be much lower with VWN5 than with PW91 (0.15 kcal/mol versus 1.26 kcal/mol from KSCED(m)). We obtained 0.47 kcal/mol (with VWN5) and 1.31 kcal/mol (with PW91) using KSCED(m). In contrast, KSCED(s, ext orth, $\nu_T = 0$)

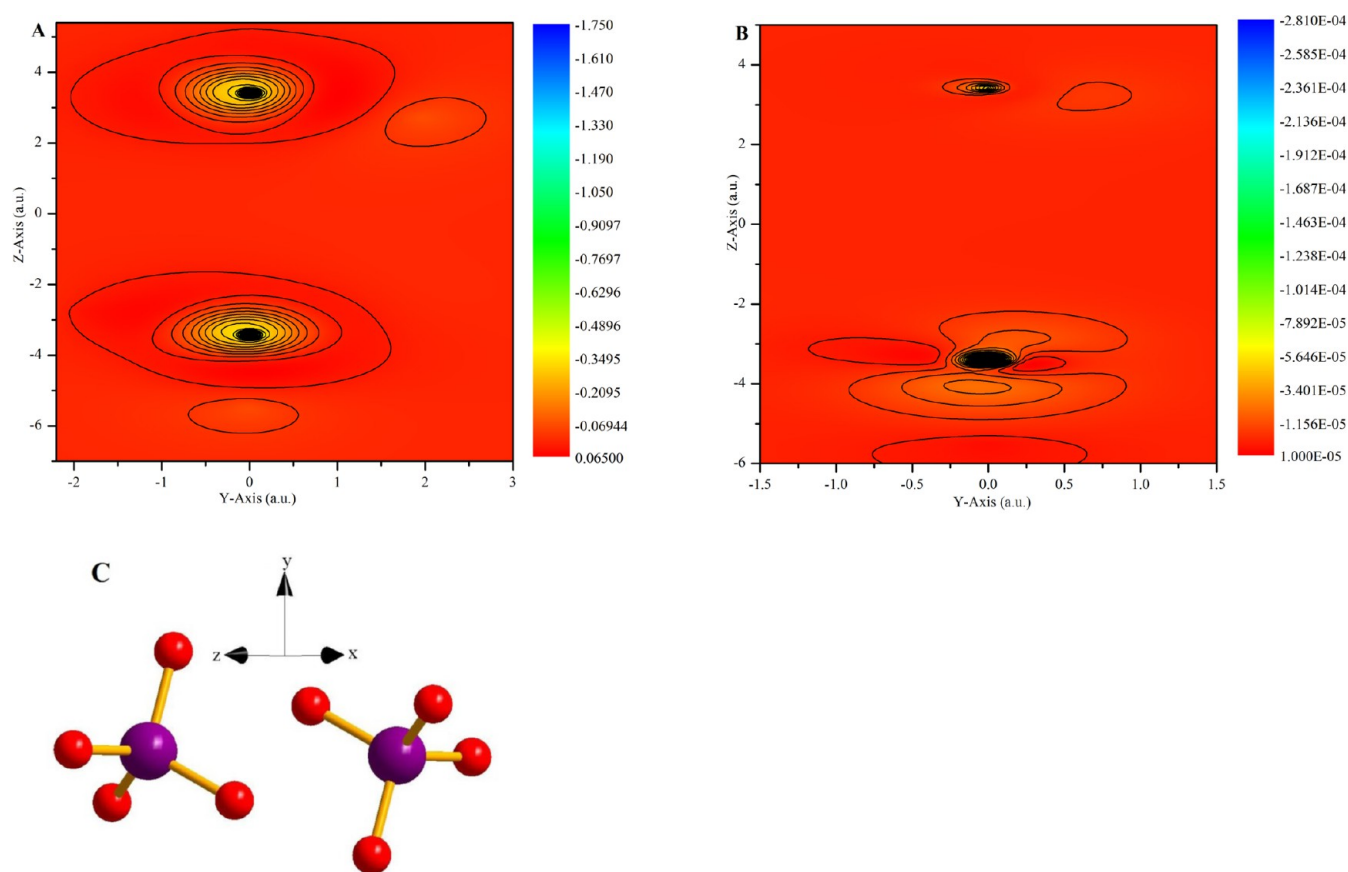


Figure 6. Density difference contour maps (yz -plane) for the $\text{CH}_4 \cdots \text{CH}_4$ complex, positioned as shown. The maps display the density differences: A = KS-DFT – KSCED(s); B = KS-DFT – KSCED(s, ext orth, $v_T = 0$). Image C is the geometry of the complex.

calculations with PW91 reproduced the KS-DFT interaction energy (5.37 kcal/mol) to within 0.01 kcal/mol.

v. $\text{CH}_4 \cdots \text{CH}_4$. The $\Delta\rho$ isocontour maps for $\text{CH}_4 \cdots \text{CH}_4$ are shown in Figure 6, obtained with the VWN5 functional. The maps are labeled A and B and represent the density differences: A = KS-DFT – KSCED(s); B = KS-DFT – KSCED(s, ext orth, $v_T = 0$). Image C specifies the geometry of the complex. The $\Delta\rho$ values on the yz -plane are shown. Density deviations can be seen to be largely within molecular regions of each of the subsystems. Charge deviation buildup is minimal at the interface between the molecular fragments, which is not surprising as the $\text{CH}_4 \cdots \text{CH}_4$ complex involves only weak van der Waals interactions.

Comparing images A and B, one sees that including external orthogonality and setting v_T to zero diminishes density deviations from on the order of 10^{-2} to 10^{-5} e/a_0^3 . Isocontours in A are shown in the range $[-1.75, +0.065]$ in steps of $4.5375 \times 10^{-2} \text{ e/a}_0^3$ whereas those in B are in the range $[-2.81 \times 10^{-4}, +1.00 \times 10^{-5}]$ in steps of $7.275 \times 10^{-6} \text{ e/a}_0^3$. The ref 42 study predicted an interaction energy of only 0.43 kcal/mol for this complex with VWN5 in KSCED(m) calculations, and the present study obtained 0.42 kcal/mol for the same calculations.

vi. *Parallel-Displaced (PD) π -Stacked $\text{C}_6\text{H}_6 \cdots \text{C}_6\text{H}_6$ Complex.* The $\Delta\rho$ isocontour and relief maps for the parallel-displaced (PD) π -stacked $\text{C}_6\text{H}_6 \cdots \text{C}_6\text{H}_6$ complex are shown in Figure 7. The maps are labeled A to C and represent the density differences: A = KS-DFT – KSCED(m); B = KS-DFT – KSCED(s); C = KS-DFT – KSCED(s, ext orth, $v_T = 0$). Image D specifies the geometry of the complex. Image A shows $\Delta\rho$ on the yz -plane (which cuts through the benzene rings), and

images B and C show $\Delta\rho$ on the xz -plane (i.e., the plane through the interface between the two benzene rings). The two benzene rings are parallel to each other; one lies on the $y = 1.8 \text{ \AA}$ xz -plane and the other is on the $y = -1.8 \text{ \AA}$ xz -plane. Hence the $y = 0$ xz -plane is the interfacial plane. This system, in the considered geometry, involves fairly strong π – π coupling. As can be seen, $\Delta\rho$ values are non-negligible at the intermolecular interface and are significant within the subsystems (image A in Figure 7). Image B corroborates that there is a fairly significant accumulation of electron density deviation (on the order of 10^{-3} e/a_0^3) at the interface between the molecular subsystems (in the absence of setting $v_T = 0$).

Image C of Figure 7 shows that when external orthogonality was enforced within the new embedding program and the nonadditive kinetic potential was set to zero, density deviations of KSCED from KS-DFT became negligible, decreasing from on the order of 10^{-3} e/a_0^3 in B to on the order of 10^{-8} e/a_0^3 in C. The interaction energy of the (PD) π -stacked $\text{C}_6\text{H}_6 \cdots \text{C}_6\text{H}_6$ complex was determined in ref 42 to be as large as 1.97 kcal/mol less than the KS-DFT value of 2.78 kcal/mol, with the VWN5 functional in KSCED(s) calculations with the aug-cc-pVTZ basis set. In the present study, using a cc-pVDZ basis set and VWN5 in the new embedding program, KSCED(s, ext orth, $v_T = 0$) reproduced the KS-DFT interaction energy of 2.66 kcal/mol to the fifth decimal place.

vii. $\text{Li}^+ \cdots \text{H}_2\text{O}$ and $\text{F}^- \cdots \text{H}_2\text{O}$. Density deviation calculations for $\text{Li}^+ \cdots \text{H}_2\text{O}$ and $\text{F}^- \cdots \text{H}_2\text{O}$ complexes, similar to the earlier examined complexes, are shown in Figures 8 and 9, respectively. All densities were computed with the VWN functional. Maps A and B of both figures represent the density

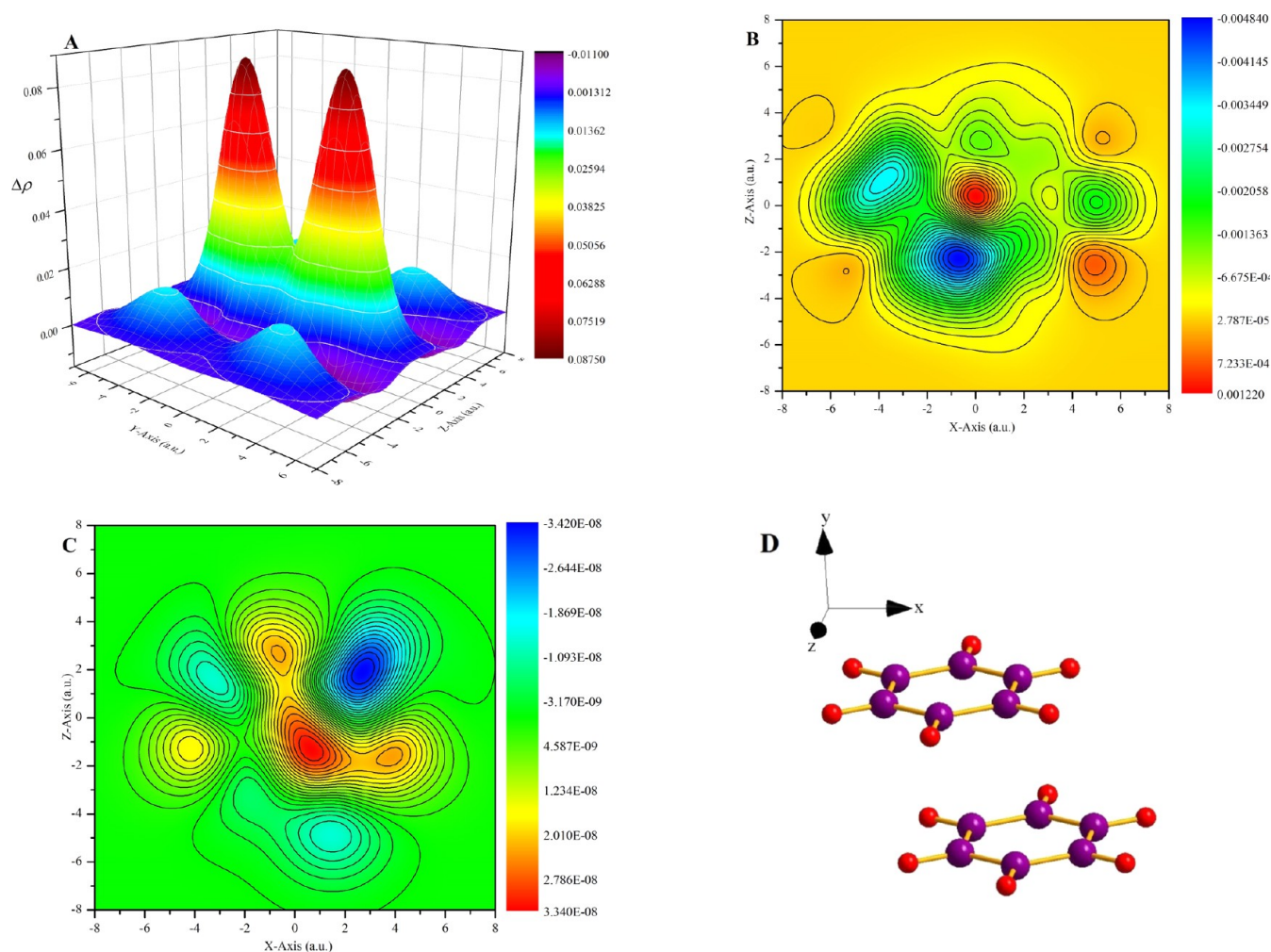


Figure 7. Density difference relief and contour maps for the parallel displaced (PD) π -stacked $\text{C}_6\text{H}_6 \cdots \text{C}_6\text{H}_6$ complex, positioned as shown. The maps are for the density differences: A = KS-DFT – KSCED(m); B = KS-DFT – KSCED(s); C = KS-DFT – KSCED(s, ext orth, $\nu_T = 0$). In Image A, $\Delta\rho$ on the yz-plane is shown; in B and C, $\Delta\rho$ on the xz-plane is shown. Image D shows the geometry of the complex.

differences: A = KS-DFT – KSCED(s); B = KS-DFT – KSCED(s, ext orth, $\nu_T = 0$). Images A of both Figures 8 and 9 show a buildup of electron density in the boundary region between Li^+ and H_2O , and between F^- and H_2O . Accounting for external orbital orthogonality and setting $\nu_T = 0$ decreases density deviations significantly to nearly zero for the $\text{Li}^+ \cdots \text{H}_2\text{O}$ complex (image B of Figure 8) and to the order of 10^{-6} e/a_0^3 for the $\text{F}^- \cdots \text{H}_2\text{O}$ complex.

In addition to the DFT-in-DFT vs KS-DFT calculations discussed thus far, images C and D of Figure 8 summarize the results of calculations in which complex densities are compared to the densities of isolated molecules. These calculations are similar to those previously reported in ref 39 (cf. the first two images in Figure 4) and serve in part as additional verification of our code. Specifically, C = $\Delta\rho^{\text{KS}} = (\text{Ffull system KS-DFT density}) - (\text{sum of densities of isolated } \text{Li}^+ \text{ and } \text{H}_2\text{O} \text{ fragments obtained from KS-DFT})$ and D = $\Delta\rho^{\text{KSCED(m)}} = (\text{full system KSCED(m) density}) - (\text{sum of densities of isolated } \text{Li}^+ \text{ and } \text{H}_2\text{O} \text{ fragments obtained from KS-DFT})$. We report isocontours in images C and D in the same range $[-0.05, +0.05]$ and step size ($2.5 \times 10^{-3} \text{ e/a}_0^3$) as in Figure 4 of ref 39. The two sets of images (C and D here and Figure 4 of ref 39) are in good agreement. Images E of Figure 8 and C of Figure 9

specify the geometries of $\text{Li}^+ \cdots \text{H}_2\text{O}$ and $\text{F}^- \cdots \text{H}_2\text{O}$ used in the calculations, respectively.

Displayed in Figure 10 are the PECs for the separation of $\text{Li}^+ \cdots \text{H}_2\text{O}$ into Li^+ and H_2O fragments, computed using the VWN functional. Additional data describing the curves, and those obtained using the PW91 functional, are in Table 1. Although the figure and table both show a fairly strong interaction between the Li^+ and H_2O fragments (i.e., all methods predict interaction energies of at least 40 kcal/mol), there are marked differences in KSCED(m) and KSCED(s) results compared to the reference KS-DFT values. KSCED(m) and KSCED(s), using VWN, predict equilibrium separations that are 0.16 and 0.13 Å shorter than does KS-DFT, respectively. The KSCED(s) dissociation energy is 3.78 kcal/mol more, whereas that from KSCED(m) is 5.34 kcal/mol less than the reference KS-DFT value using VWN. These trends are repeated in the case of PW91 where equilibrium separations are 0.24 and 0.22 Å less, whereas dissociation energies are 0.82 kcal/mol less and 8.54 kcal/mol more than KS-DFT values for KSCED(m) and KSCED(s), respectively. As can be seen in Figure 10, the KSCED(e) curve is very similar to that from KSCED(s) calculations (N.B. the purple KSCED(e) and red KSCED(s) curves in Figure 10 are virtually indistinguishable). Irrespective of functional type, enforcing external orbital

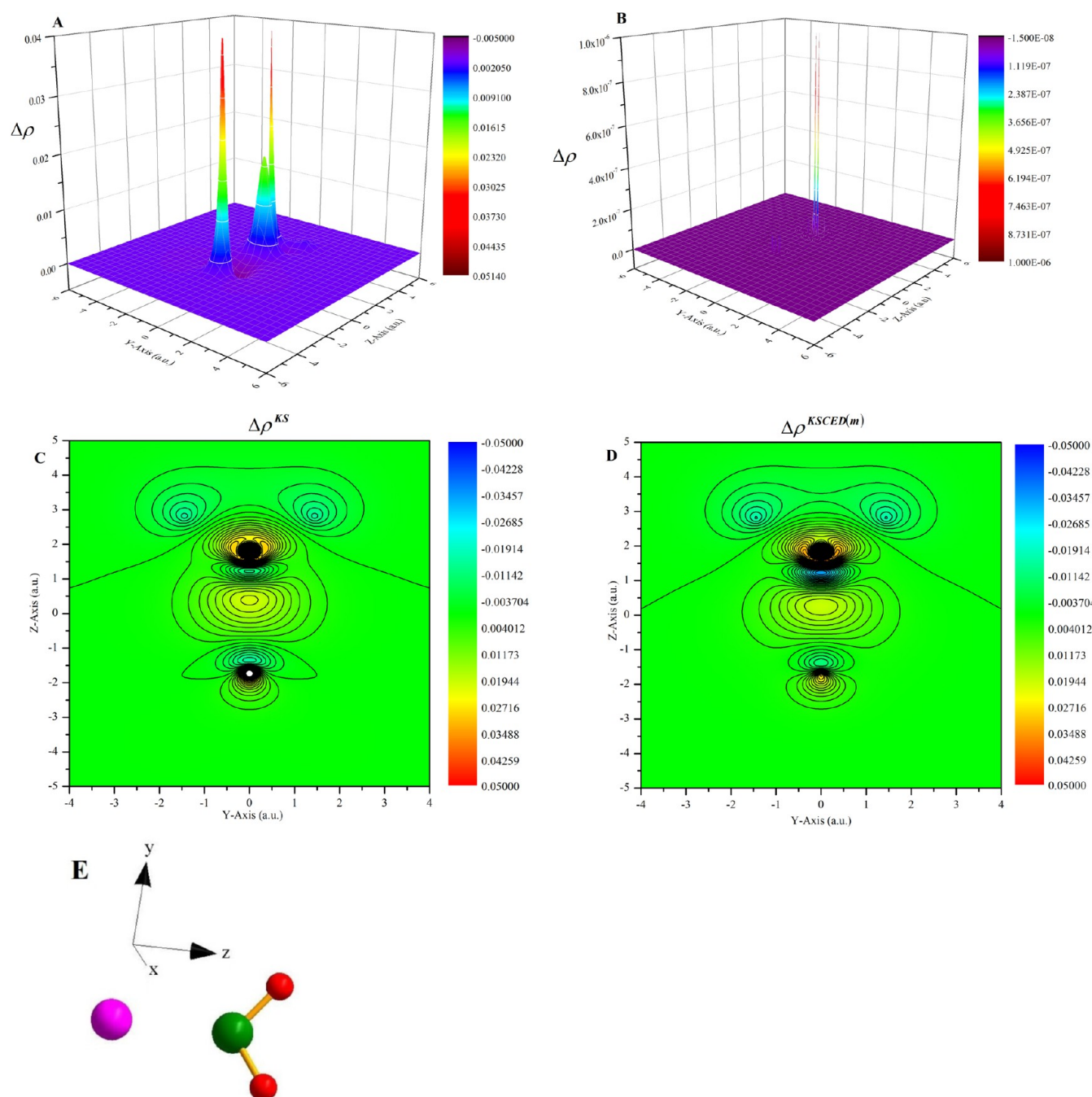


Figure 8. Density difference relief and contour maps (yz -plane) for the $\text{Li}^+\cdots\text{H}_2\text{O}$ complex, positioned as shown. The maps display the density differences: A = KS-DFT – KSCED(s); B = KS-DFT – KSCED(s, ext orth, $\nu_T = 0$); C = $\Delta\rho^{\text{KS}}$ = (full system KS-DFT density) – (sum of densities of isolated Li^+ and H_2O fragments obtained from KS-DFT); D = $\Delta\rho^{\text{KSCED(m)}}$ = (full system KSCED(m) density) – (sum of densities of isolated Li^+ and H_2O fragments obtained from KS-DFT). Image E shows the geometry of the complex.

orthogonality and zeroing the nonadditive kinetic potential ($\nu_T = 0$) leads, in the present case, to KSCED(s, ext orth, $\nu_T = 0$) results that are the same as those from KS-DFT (i.e., compare the blue and black curves in Figure 10; also see Table 1 where equilibrium separations and interaction energies are the same for KSCED(s, ext orth, $\nu_T = 0$) and KS-DFT. Note that the black KS-DFT curve in Figure 10 is additionally marked with a symbol for each data point. In addition, the KSCED(e, ext orth, $\nu_T = 0$) curve in Figure 10 is also very similar to the reference KS-DFT curve, agreeing with the equilibrium separation (1.82 Å) to within 0.01 Å and with the dissociation energy to within

0.28 kcal/mol. Similar results are obtained with the PW91 functional (not shown).

b. Potential Energy Curves (PECs) of $\text{HF}\cdots\text{HF}$ and $\text{He}\cdots$

Ne. Figure 11 shows PECs for the dissociation of the $\text{HF}\cdots\text{HF}$ complex into monomers, computed using the VWN5 functional; additional data, and those obtained using the PW91 functional, can be found in Table 1. The KS-DFT data in Figure 11 are marked with a symbol to indicate where they lie because the interpolated curve is completely obscured by the KSCED(s, ext orth, $\nu_T = 0$) curve. Unlike the $\text{Li}^+\cdots\text{H}_2\text{O}$ case for which equilibrium separations of KSCED(s) and KSCED(m)

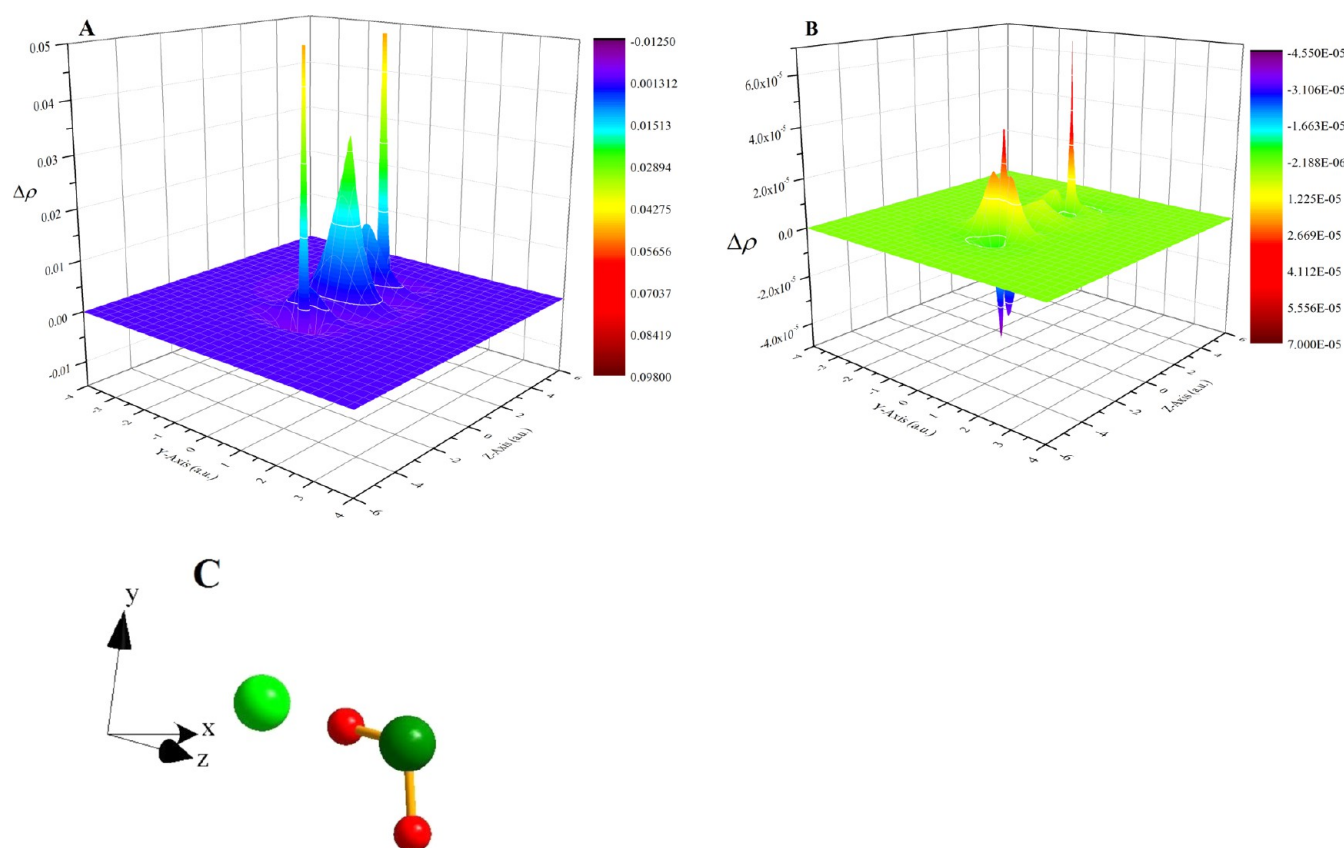


Figure 9. Density difference relief maps (yz -plane) for the $\text{H}_2\text{O}\cdots\text{F}^-$ complex, positioned as shown. The maps display the density differences: A = KS-DFT – KSCED(s); B = KS-DFT – KSCED(s, ext orth, $\nu_T = 0$). Image C shows the geometry of the complex.

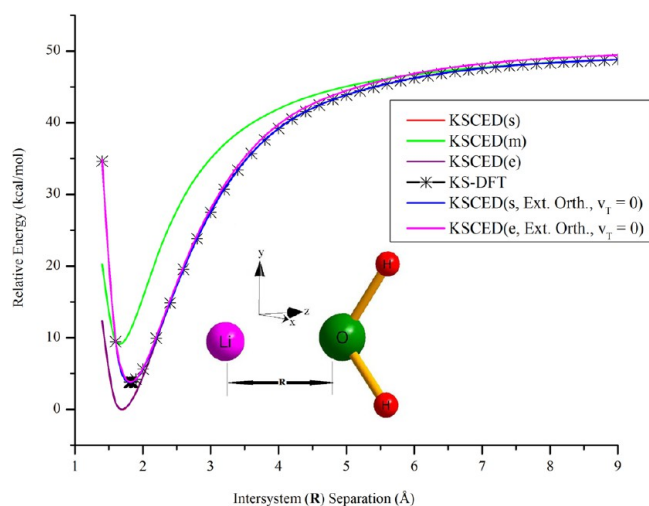


Figure 10. PECs of the $\text{Li}^+\cdots\text{H}_2\text{O}$ complex computed using the methods shown in the inset. The geometry of ref 39 was used, and the $\text{Li}^+\cdots\text{O}$ intersystem separation (R) was varied.

were less than the reference KS-DFT value, the situation is reversed in the case of $\text{HF}\cdots\text{HF}$ where DFT-in-DFT, without external orthogonality, is seen to predict longer equilibrium separations than KS-DFT for both VWN5 and PW91 functionals. Moreover, the dissociation energy obtained from KSCED(s) calculations of $\text{Li}^+\cdots\text{H}_2\text{O}$ using PW91 is in poorer agreement with KS-DFT than is the KSCED(m) value. The same calculations on $\text{HF}\cdots\text{HF}$ show that the dissociation energy predicted by KSCED(s) is in better agreement with KS-

DFT than is the interaction energy from KSCED(m). Furthermore, the KSCED(s) interaction energy for $\text{Li}^+\cdots\text{H}_2\text{O}$ (using VWN) is in better agreement with KS-DFT than is the KSCED(m) value. Also noteworthy is that deviations in equilibrium separation and dissociation energy increase from the LDA (VWN) value to the GGA (PW91) value in the case of $\text{Li}^+\cdots\text{H}_2\text{O}$, using KSCED(s), whereas the opposite effect is seen in the case of $\text{HF}\cdots\text{HF}$ (Table 1).

As can be seen in Figure 11 and in Table 1, enforcing external orbital orthogonality and setting $\nu_T = 0$ leads to KSCED(s, ext orth, $\nu_T = 0$) results that are the same as those from the reference KS-DFT for both VWN5 and PW91 functionals. On the other hand, failure to enforce the vanishing of the nonadditive kinetic potential (while enforcing external orthogonality) leads to essentially worse PECs than those from conventional DFT-in-DFT (compare the blue curve in Figure 11 to the red and green ones).

Figure 12 contains PECs of the separation of $\text{He}\cdots\text{Ne}$ into atoms, obtained with the PW91 functional. Once more, the KS-DFT data in Figure 12 are marked with a symbol because the interpolated curve is completely obscured by the KSCED(s, ext orth, $\nu_T = 0$) curve. Additional data describing the curves are in Table 1. As can be seen in Figure 12 and Table 1, KSCED(s) calculations of this complex lead to an equilibrium separation that is 0.30 Å too short and an interaction energy that is 0.19 kcal/mol too large in comparison with that for KS-DFT. On the other hand, accounting for external orthogonality in KSCED(s) without setting $\nu_T = 0$ leads to a minimum that is 0.39 Å too long and an interaction energy that is 0.17 kcal/mol too low compared to KS-DFT values. As before, enforcing

Table 1. Equilibrium Separations (R_e) and Interaction Energies (D_e) of the $\text{Li}^+\cdots\text{H}_2\text{O}$, $\text{HF}\cdots\text{HF}$, and $\text{He}\cdots\text{Ne}$ Complexes Computed Using Various Methods and the VWN, VWN5, and PW91 Functionals

complex	method	functional type, equilibrium separation, and interaction energy			
		VWN		PW91	
		R_e (Å)	D_e (kcal/mol)	R_e (Å)	D_e (kcal/mol)
$\text{Li}^+\cdots\text{H}_2\text{O}$	KSCED(s)	1.69	49.12	1.63	51.66
	KSCED(m)	1.66	40.00	1.61	42.30
	KSCED(e)	1.70	49.11		
	KSCED(e, ext orth, $\nu_T = 0$)	1.82	45.62	1.86	42.95
	KSCED(s, ext orth, $\nu_T = 0$)	1.82	45.34	1.85	43.12
	KS-DFT	1.82	45.34	1.85	43.12
$\text{HF}\cdots\text{HF}$		functional type, equilibrium separation, and interaction energy			
		VWN5		PW91	
		R_e (Å)	D_e (kcal/mol)	R_e (Å)	D_e (kcal/mol)
	KSCED(s)	1.79	4.00	1.78	4.84
	KSCED(m)	1.80	3.71	1.79	4.60
	KSCED(s, ext orth)	3.00	1.08	2.90	1.25
$\text{He}\cdots\text{Ne}$	KSCED(s, ext orth, $\nu_T = 0$)	1.58	7.91	1.76	4.93
	KS-DFT	1.58	7.91	1.76	4.93
		functional type, equilibrium separation, and interaction energy			
		PW91			
		R_e (Å)	D_e (kcal/mol)	R_e (Å)	D_e (kcal/mol)
	KSCED(s)			2.53	0.48
	KSCED(s, ext orth)			3.22	0.12
	KSCED(s, ext orth, $\nu_T = 0$)			2.83	0.29
	KS-DFT			2.83	0.29

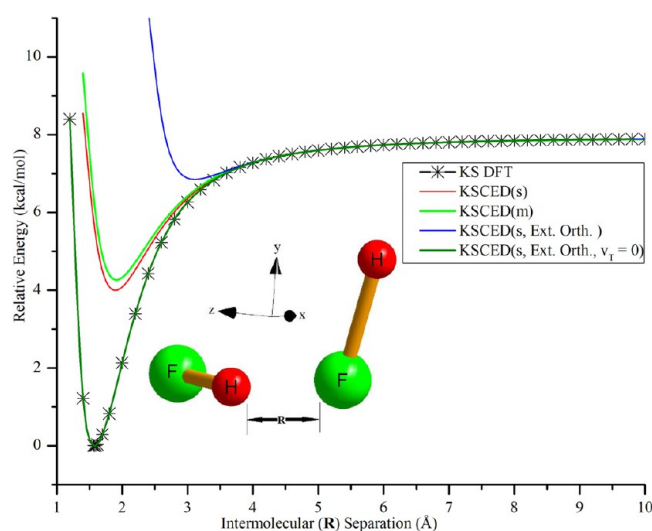


Figure 11. PECs of the $\text{HF}\cdots\text{HF}$ complex computed using the methods shown in the inset. The optimized geometry of ref S3 was used, and the F \cdots H intermolecular separation (R) was varied.

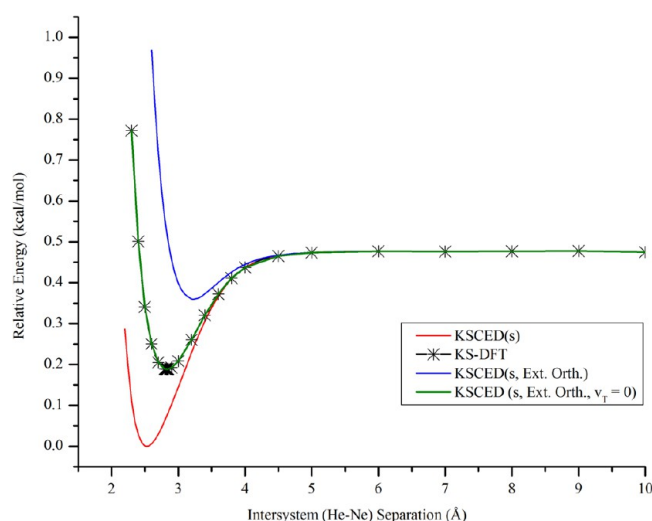


Figure 12. PECs of the $\text{He}\cdots\text{Ne}$ complex computed using the methods shown in the inset.

external orthogonality and setting $\nu_T = 0$ within the new embedding theory reproduces reference KS-DFT results more-or-less exactly.

Table 2 shows the effect of varying the fraction of the single determinant exchange in hybrid functionals on the disparity between KS-DFT and DFT-in-DFT embedding total energies. The self-interaction of the electrons has been thought to contribute to inaccuracies in conventional DFT-in-DFT embedding theory and the use of hybrid functionals was suggested^{27,28} as a means of remedying the situation. If this were indeed the case, then the accuracy of embedding theory energies should improve with increasing fraction of single determinant exchange. In the present study, we performed calculations on the $\text{Li}^+\cdots\text{Be}$ and $\text{H}_2\text{O}\cdots\text{H}_2\text{O}$ complexes using the hybrid functionals indicated in Table 2 in KSCED(s, ext orth, with and without setting $\nu_T = 0$) and KS-DFT calculations, while varying the fraction of single determinant exchange in the functionals. From the fifth column of Table 2, it can be seen that simply increasing the fraction of single determinant exchange, without setting the nonadditive kinetic potential to 0, increases the discrepancy between KS-DFT and KSCED(s) energies for all hybrid functionals tested with the $\text{H}_2\text{O}\cdots\text{H}_2\text{O}$ and $\text{Li}^+\cdots\text{Be}$ systems. This is clearly contrary to the predicted effect of exact single determinant exchange in DFT-in-DFT. On the other hand, the new embedding method, KSCED(s, ext orth, $\nu_T = 0$), is shown (last column of Table 2) to be more-or-less insensitive to variations in the fraction of single determinant exchange, virtually reproducing the reference KS-DFT energies for the different fractions in all tested hybrid functionals.

IV. CONCLUSIONS

A novel approach to DFT-in-DFT embedding that reproduces conventional KS-DFT energy results nearly exactly and leads to negligible electron density differences has been presented and numerically assessed on some molecular complexes. The new DFT-in-DFT embedding scheme, which is denoted KSCED(x, ext orth, $\nu_T = 0$) (where x = s, m or e designates type of one-particle basis), enforces intersystem orbital orthogonality but does not require any calculations on the entire molecule. External orbital orthogonality is included as an additional constraint in the coupled Euler–Lagrange equations that are

Table 2. Effect of Fraction of Single Determinant Exchange in Hybrid Functionals on the Discrepancy between the KSCED(s) Energy in Comparison with That of KS-DFT^a

fraction single determinant exchange	total energies (au)			energy differences (au)	
	KS-DFT	KSCED(s)	KSCED(s, ext orth, $\nu_T = 0$)	KS-DFT – KSCED(s)	KS-DFT – KSCED(s, ext orth, $\nu_T = 0$)
Li ⁺ ...Be (B3LYP)					
0.04	–21.8916713604	–21.9104898680	–21.8916713604	0.0188185076	0 ^b
0.10	–21.9262759753	–21.9462654855	–21.9262759753	0.0199895102	0
0.20	–21.9840841552	–22.0061898917	–21.9840841551	0.0221057365	0
0.22	–21.9956656723	–22.0182226961	–21.9956656723	0.0225570238	0
0.24	–22.0072537681	–22.0302724205	–22.0072537681	0.0230186524	0
0.26	–22.0188484222	–22.0423395201	–22.0188484222	0.0234910979	0
0.28	–22.0304496146	–22.0544244786	–22.0304496146	0.0239748640	0
0.30	–22.0420573254	–22.0665278092	–22.0420573254	0.0244704839	0
0.32	–22.0536715349	–22.0786500587	–22.0536715350	0.0249785237	0
0.34	–22.0652922239	–22.0907918087	–22.0652922239	0.0254995848	0
0.36	–22.0769193729	–22.1029536793	–22.0769193729	0.0260343063	0
0.40	–22.1001929757	–22.1273404724	–22.1001929757	0.0271474967	0
H ₂ O...H ₂ O (BHandHLYP)					
0.3	–152.8710402674	–152.8743717310	–152.8710402673	0.0033314637	–2.3 (–11)
0.4	–152.8609383261	–152.8655505198	–152.8609383261	0.0046121937	1 (–12)
0.5	–152.8513866536	–152.8573340661	–152.8513866536	0.0059474124	–1 (–12)
0.6	–152.84236 87865	–152.84972 83797	–152.84236 87865	0.00735 95932	0
0.7	–152.83386 92765	–152.84274 73490	–152.83386 92765	0.00887 80725	2 (12)
0.8	–152.82587 35848	–152.83641 66927	–152.82587 35848	0.01054 31079	–1 (–12)
H ₂ O...H ₂ O (B1B95)					
0.28	–152.87130 10656	–152.87421 62934	–152.87130 10656	0.00291 52277	–1.6 (–11)
0.38	–152.86156 28264	–152.865710 1120	–152.86156 28264	0.00414 72856	–2 (–12)
0.48	–152.85237 35896	–152.85779 92151	–152.85237 35896	0.00542 56255	–1 (–12)
0.58	–152.84371 67076	–152.85048 71278	–152.84371 67076	0.00677 04202	–1 (–12)
0.68	–152.83557 65807	–152.84378 41184	–152.83557 65807	0.00820 75377	–1 (–12)
H ₂ O...H ₂ O (MPW3LYP)					
0.2	–152.93831 87373	–152.94147 81972	–152.93831 87373	0.00315 94599	–1.4 (–11)
0.3	–153.10037 31747	–153.10473 11519	–153.10037 31747	0.00435 79772	–1 (–12)
0.4	–153.26316 73599	–153.26873 51985	–153.26316 73599	0.00556 78385	–2 (–12)
0.5	–153.42668 53093	–153.43349 01318	–153.42668 53093	0.00680 48225	0
0.6	–153.59091 21148	–153.59900 02810	–153.59091 21148	0.00808 81662	–1 (–12)

^aAll calculations were done with the aug-cc-pVTZ basis. The Li⁺...Be calculations were done at 2.6 Å. H₂O...H₂O calculations used the optimized geometry of ref 53. ^bZero denotes less than 1×10^{-12} .

solved to self-consistency for the subsystems. In this new embedding approach, the nonadditive kinetic potential (ν_T), which is the main source of errors in subsystem DFT embedding methods in general, can be set without approximation to its theoretical value of zero. Thus, the new approach does not rely on kinetic energy functionals and is unaffected by their inaccuracies. Irrespective of functional type, KSCED(s, ext orth, $\nu_T = 0$) calculations were found to reproduce reference KS-DFT results more-or-less exactly. For all studied systems, which span interaction strengths from ca. 0.3 kcal/mol (for He...Ne) to ca. 40 kcal/mol (for Li⁺...H₂O), reference supermolecular KS-DFT total energies were reproduced to at least the seventh decimal place, irrespective of intersystem interaction strengths or the type of DFT functional used. To our knowledge, no previous version of DFT-in-DFT that does not require a supermolecular KS-DFT calculation matches the accuracies of the data reported in the present work from the new variant of DFT-in-DFT embedding theory.

Extending the usual monomer basis expansion, KSCED(m), to include basis functions in the complementary subsystem centered on atoms close to the interface, led to a significantly less computationally intensive approach, to which we refer to as

“extended monomer” and designate KSCED(e). Calculations on the considered systems with the extended monomer basis gave results close to those obtained with the supermolecular basis, KSCED(s), and significantly better than calculations with the monomer basis, KSCED(m). Determination of the extent of the interface may be more difficult in systems in which orbitals cannot be localized. For the considered systems in which subsystem seams were unambiguous, KSCED(e, ext orth, $\nu_T = 0$) calculations were found to give results that were closely related to those from KSCED(s, ext orth, $\nu_T = 0$) and from reference KS-DFT and is our recommendation for DFT-in-DFT embedding calculations.

Whereas the pilot computer program implementing the new DFT-in-DFT embedding theory does not allow meaningful timing comparisons (vis-à-vis KS-DFT) to be made, a few observations concerning numerical characteristics are appropriate. For the systems considered herein, we find that two or three “freeze-and-thaw” cycles were needed to bring the subsystems into equilibrium (i.e., chemical potential, cf. eq 12, converged to 1×10^{-6}). For each subsystem KS-DFT calculation, convergence (to 1×10^{-8} in the gradient) was achieved in about ca. 8 iterations, whereas KS-DFT calculations

on the entire system would take 10–15 iterations. Consequently, the new DFT-in-DFT embedding theory required about twice as many Fock matrix constructions and diagonalizations as did ordinary KS-DFT calculations. Of course, each of the subsystem Fock constructions and diagonalizations using the extended monomer basis, (e), involved significantly smaller dimensions than did KS-DFT calculations on the whole system. Clearly, characterization and optimization of numerical algorithms, for a wider range of examples, is a next step in the development of this method.

Although KSCED(s or e, ext orth, $\nu_T = 0$) calculations more-or-less exactly reproduce KS-DFT densities on the entire molecule, a correlation between KS-DFT and DFT-in-DFT density deviations, when ν_T was calculated using approximate functionals, and interaction strength was observed. Not surprisingly, they tend to be large for strongly interacting systems (such as $\text{Li}^+ \cdots \text{H}_2\text{O}$ or $\text{H}_2\text{O} \cdots \text{F}^-$) and small for weakly interacting systems (such as $\text{F}_2 \cdots \text{C}_2\text{H}_4$). In particular, there is some electron density in the interfacial region between subsystems, which embedding theory fails to account for, and this density correlates not only with the strength of interaction between the subsystems but also with their polarizability; e.g., the electron density error was found to be negligible at the interface between CH_4 molecules in the $\text{CH}_4 \cdots \text{CH}_4$ complex but substantial in complexes such as the parallel displaced (PD) π -stacked $\text{C}_6\text{H}_6 \cdots \text{C}_6\text{H}_6$. Although not of principal concern here, as KSCED(s or e, ext orth, $\nu_T = 0$) densities essentially are the same as those of KS-DFT, it might be of interest to develop a more systematic understanding of these density deviations.

Because the agreement with whole molecule KS-DFT obtained with the new embedding protocol did not depend on the functionals used, the new embedding approach appears to remedy the “lack of tendency” in conventional DFT-in-DFT embedding.^{26,64} In some instances, conventional DFT-in-DFT embedding results with GGA functionals are better than those from LDA (in comparison with reference KS-DFT results) and in other instances, they are worse. Because of the essentially exact agreement of KSCED(s, ext orth, $\nu_T = 0$) with KS-DFT, accuracy tendencies of KS-DFT hold in the new method.

AUTHOR INFORMATION

Corresponding Author

*M. R. Hoffmann. E-mail: mhoffmann@chem.und.edu. Phone: (+1) 701-777-2742. Fax: (+1) 701-777-2331.

Notes

The authors declare no competing financial interest.

ACKNOWLEDGMENTS

This work was supported with funds from the National Science Foundation (Grant No. EPS-0814442) for which we are grateful. M.R.H. is grateful to Andreas Savin and Trygve Helgaker for earlier discussions on DFT embedding, and on participants in the CECAM Workshop: Density-Based Embedding for Multiscale Simulations (and, in particular, organizers Tomasz Wesolowski and Christoph Jacob) for critical input.

REFERENCES

- (1) Foster, J. M.; Boys, S. F. Canonical Configurational Interaction Procedure. *Rev. Mod. Phys.* **1960**, *32*, 300–302. Boys, S. F. In *Quantum Theory of Atoms, Molecules and the Solid State*; Lowdin, P. O., Ed.; Academic Press: New York, 1966; p 253.
- (2) Edmiston, C.; Ruedenberg, K. Localized Atomic and Molecular Orbitals. *Rev. Mod. Phys.* **1963**, *35*, 457–465. Edmiston, C.; Ruedenberg, K. Localized Atomic and Molecular Orbitals II. *J. Chem. Phys.* **1965**, *43*, S97–S116.
- (3) Reed, A. E.; Weinhold, F. Natural Localized Molecular Orbitals. *J. Chem. Phys.* **1985**, *83*, 1736–1740.
- (4) Wesolowski, T. A. Embedding a Multideterminantal Wave Function in an Orbital-Free Environment. *Phys. Rev. A* **2008**, *77*, 012504/1–9.
- (5) Khait, Y. G.; Hoffmann, M. R. Embedding Theory for Excited States. *J. Chem. Phys.* **2010**, *133*, 044107/1–6.
- (6) Huang, C.; Pavone, M.; Carter, E. A. Quantum Mechanical Embedding Theory Based on a Unique Embedding Potential. *J. Chem. Phys.* **2011**, *134*, 154110/1–11.
- (7) Huang, C.; Carter, E. A. Potential-Functional Embedding Theory for Molecules and Materials. *J. Chem. Phys.* **2011**, *135*, 194104/1–17.
- (8) Jacob, C. R.; Neugebauer, J.; Visscher, L. A Flexible Implementation of Frozen-Density Embedding for use in Multilevel Simulations. *J. Comput. Chem.* **2008**, *29*, 1011–1018.
- (9) Wesolowski, T. A.; Warshel, A. Frozen Density Functional Approach for Ab Initio Calculations of Solvated Molecules. *J. Phys. Chem.* **1993**, *97*, 8050–8053.
- (10) Wesolowski, T. A.; Weber, J. Kohn-Sham Equations with Constrained Electron Density: An Iterative Evaluation of the Ground-State Electron Density of Interacting Molecules. *Chem. Phys. Lett.* **1996**, *248*, 71–76.
- (11) Govind, N.; Wang, Y. A.; da Silva, A. J. R.; Carter, E. A. Accurate Ab Initio Energetics of Extended Systems via Explicit Correlation Embedded in a Density Functional Environment. *Chem. Phys. Lett.* **1998**, *295*, 129–134.
- (12) Cortona, P. Self-Consistently Determined Properties of Solids without Band-Structure Calculations. *Phys. Rev. B* **1991**, *44*, 8454–8458.
- (13) Johnson, M. D.; Subbaswamy, K. R.; Senatore, G. Hyperpolarizabilities of Alkali Halide Crystals Using the Local-Density Approximation. *Phys. Rev. B* **1987**, *36*, 9202–9211.
- (14) Wesolowski, T. A. One Electron Equations for Embedded Electron Density: Challenge for Theory and Practical Payoffs in Multilevel Modelling of Complex Polyatomic Systems. In *Computational Chemistry: Reviews of Current Trends*; Leszczynski, J., Ed.; World Scientific: Singapore, 2006; Vol. 10, pp 1–82.
- (15) Neugebauer, J.; Jacob, Ch. R.; Wesolowski, T. A.; Baerends, E. J. An Explicit Quantum Chemical Method for Modeling Large Solvation Shells Applied to Aminocoumarin C151. *J. Phys. Chem. A* **2005**, *109*, 7805–7814.
- (16) Jacob, Ch. R.; Neugebauer, J.; Jensen, L.; Visscher, L. Comparison of Frozen-Density Embedding and Discrete Reaction Field Solvent Models for Molecular Properties. *Phys. Chem. Chem. Phys.* **2006**, *8*, 2349–2359.
- (17) Gritsenko, O. V.; Visscher, L. Density-Orbital Embedding Theory. *Phys. Rev. A* **2010**, *82*, 032519/1–4.
- (18) Lembarki, A.; Chermette, H. Obtaining a Gradient-Corrected Kinetic-Energy Functional from the Perdew-Wang Exchange Functional. *Phys. Rev. A* **1994**, *50*, 5328–5331.
- (19) Wesolowski, T. A. Density Functional Theory with Approximate Kinetic Energy Functionals Applied to Hydrogen Bonds. *J. Chem. Phys.* **1997**, *106*, 8516–8526.
- (20) Jacob, Ch. R.; Wesolowski, T. A.; Visscher, L. Orbital-Free Embedding Applied to the Calculation of Induced Dipole Moments in $\text{CO}_2 \cdots \text{X}$ (X = He, Ne, Ar, Kr, Xe, Hg) van der Waals Complexes. *J. Chem. Phys.* **2005**, *123*, 174104/1–11.
- (21) Götz, A. W.; Beyhan, S. M.; Visscher, L. Performance of Kinetic Energy Functionals for Interaction Energies in a Subsystem Formulation of Density Functional Theory. *J. Chem. Theory Comput.* **2009**, *5*, 3161–3174.
- (22) Wesolowski, T. A.; Ellinger, Y.; Weber, J. Density Functional Theory with an Approximate Kinetic Energy Functional Applied to Study Structure and Stability of Weak van der Waals Complexes. *J. Chem. Phys.* **1998**, *108*, 6078–6083.

- (23) Fux, S.; Kiewisch, K.; Jacob, Ch. R.; Neugebauer, J.; Reiher, M. Analysis of Electron Density Distributions from Subsystem Density Functional Theory Applied to Coordination Bonds. *Chem. Phys. Lett.* **2008**, *461*, 353–359.
- (24) Beyhan, S. M.; Götz, A. W.; Jacob, Ch. R.; Visscher, L. The Weak Covalent Bond in NgAuF (Ng= Ar, Kr, Xe): A Challenge for Subsystem Density Functional Theory. *J. Chem. Phys.* **2010**, *132*, 044114/1–9.
- (25) Fux, S.; Jacob, Ch. R.; Neugebauer, J.; Visscher, L.; Reiher, M. Accurate Frozen-Density Embedding Potentials as a First Step towards a Subsystem Description of Covalent Bonds. *J. Chem. Phys.* **2010**, *132*, 164101/1–18.
- (26) Dulak, M.; Kamiński, J. W.; Wesolowski, T. A. Equilibrium Geometries of Noncovalently Bound Intermolecular Complexes Derived from Subsystem Formulation of Density Functional Theory. *J. Chem. Theory Comput.* **2007**, *3*, 735–745.
- (27) Laricchia, S.; Fabiano, E.; Della Sala, F. Frozen Density Embedding with Hybrid Functionals. *J. Chem. Phys.* **2010**, *133*, 164111/1–11.
- (28) Laricchia, S.; Fabiano, E.; Della Sala, F. Semilocal and Hybrid Density Embedding Calculations of Ground-State Charge-Transfer Complexes. *J. Chem. Phys.* **2013**, *138*, 124112/1–12.
- (29) Becke, A. D. Density-Functional Thermochemistry. IV. A New Dynamical Correlation Functional and Implications for Exact-Exchange Mixing. *J. Chem. Phys.* **1996**, *104*, 1040–1046.
- (30) Zhao, Y.; Truhlar, D. G. Hybrid Meta Density Functional Theory Methods for Thermochemistry, Thermochemical Kinetics, and Noncovalent Interactions: the MPW1B95 and MPWB1K Models and Comparative Assessments for Hydrogen Bonding and van der Waals Interactions. *J. Phys. Chem. A* **2004**, *108*, 6908–6918.
- (31) Becke, A. D. A New Mixing of Hartree-Fock and Local Density-Functional Theories. *J. Chem. Phys.* **1993**, *98*, 1372–1377.
- (32) Goodpaster, J. D.; Ananth, N.; Manby, F. R.; Miller, T. F. Exact Nonadditive Kinetic Potentials for Embedded Density Functional Theory. *J. Chem. Phys.* **2010**, *133*, 084103/1–10.
- (33) Elliott, P.; Burke, K.; Cohen, M. H.; Wasserman, A. Partition Density Functional Theory. *Phys. Rev. A* **2010**, *82*, 024501/1–4.
- (34) Wu, Q.; Yang, W. A Direct Optimization Method for Calculating Density Functionals and Exchange–Correlation Potentials from Electron Densities. *J. Chem. Phys.* **2003**, *118*, 2498–2509.
- (35) Wu, Q.; Yang, W. Algebraic Equation and Iterative Optimization for the Optimized Effective Potential in Density Functional Theory. *J. Theor. Comput. Chem.* **2003**, *2*, 627–638.
- (36) Manby, F. R.; Stella, M.; Goodpaster, J. D.; Miller, T. F., III. A Simple, Exact Density-Functional-Theory Embedding Scheme. *J. Chem. Theory Comput.* **2012**, *8*, 2564–2568.
- (37) Barnard, Y. A.; Dulak, M.; Kamiński, J. W.; Wesolowski, T. A. The Energy-Differences Based Exact Criterion for Testing Approximations to the Functional for the Kinetic Energy of Non-interacting Electrons. *J. Phys. A* **2008**, *41*, 055302/1–13.
- (38) Stefanovich, E. V.; Truong, T. N. Embedded Density Functional Approach for Calculations of Adsorption on Ionic Crystals. *J. Chem. Phys.* **1996**, *104*, 2946–2955.
- (39) Dulak, M.; Wesolowski, T. A. On the Electron Leak Problem in Orbital-Free Embedding Calculations. *J. Chem. Phys.* **2006**, *124*, 164101/1–5.
- (40) Kiewisch, K.; Eickerling, G.; Reiher, M.; Neugebauer, J. Topological Analysis of Electron Densities from Kohn-Sham and Subsystem Density Functional Theory. *J. Chem. Phys.* **2008**, *128*, 044114/1–15.
- (41) Wesolowski, T. A.; Chermette, H.; Weber, J. Accuracy of Approximate Kinetic Energy Functionals in the Model of Kohn–Sham Equations with Constrained Electron Density: The FH··NCH Complex as a Test Case. *J. Chem. Phys.* **1996**, *105*, 9182–9190.
- (42) Dulak, M.; Wesolowski, T. A. Interaction Energies in Non-Covalently Bound Intermolecular Complexes Derived using the Subsystem Formulation of Density Functional Theory. *J. Mol. Model.* **2007**, *13*, 631–642.
- (43) Vosko, S. H.; Wilk, L.; Nusair, M. Accurate Spin-Dependent Electron Liquid Correlation Energies for Local Spin Density Calculations: A Critical Analysis. *Can. J. Phys.* **1980**, *58*, 1200–1211.
- (44) Thomas, L. H. The Calculation of Atomic Fields. *Proc. Cambridge Philos. Soc.* **1927**, *23*, 542–548. Fermi, E. Unmetodo Statistico per la Determinazione di Alcune Proprieta dell'Atomo. (A Statistical Method for the Determination of Some Atomic Properties). *Rend. Acad. Maz. Lancei* **1927**, *6*, 602–607.
- (45) Perdew, J. P.; Chevary, J. A.; Vosko, S. H.; Jackson, K. A.; Pederson, M. R.; Singh, D. J.; Fiollhais, C. Atoms, Molecules, Solids, and Surfaces: Applications of the Generalized Gradient Approximation for Exchange and Correlation. *Phys. Rev. B* **1992**, *46*, 6671–6687.
- (46) Perdew, J. P.; Chevary, J. A.; Vosko, S. H.; Jackson, K. A.; Pederson, M. R.; Singh, D. J.; Fiollhais, C. Erratum: Atoms, Molecules, Solids, and Surfaces: Applications of the Generalized Gradient Approximation for Exchange and Correlation. *Phys. Rev. B* **1993**, *48*, 4978–4978.
- (47) Khait, Y. G.; Hoffmann, M. R. On the Orthogonality of Orbitals in Subsystem Kohn-Sham Density Functional Theory. *Annu. Rep. Comput. Chem.* **2012**, *8*, 53–70.
- (48) Hohenberg, P.; Kohn, W. Inhomogeneous Electron Gas. *Phys. Rev. B* **1964**, *136*, 864–871.
- (49) Levy, M. Universal Variational Functionals of Electron Densities, First-Order Density Matrices, and Natural Spin-Orbitals and Solution of the V-Representability Problem. *Proc. Natl. Acad. Sci. U. S. A.* **1979**, *76*, 6062–6065.
- (50) Kohn, W.; Sham, L. J. Self-Consistent Equations Including Exchange and Correlation Effects. *Phys. Rev. A* **1965**, *140*, 1133–1138.
- (51) Harriman, J. E. Orthonormal Orbitals for the Representation of an Arbitrary Density. *Phys. Rev. A* **1981**, *24*, 680–682.
- (52) Goerling, A. Orbital- and State-Dependent Functionals in Density-Functional Theory. *J. Chem. Phys.* **2005**, *123*, 062203/1–16.
- (53) Zhao, Y.; Truhlar, D. G. Benchmark Databases for Nonbonded Interactions and their Use to test Density Functional Theory. *J. Chem. Theory Comput.* **2005**, *1*, 415–432.
- (54) Kendall, R. A.; Dunning, T. H.; Harrison, R. J. Electron Affinities of the First-Row Atoms Revisited. Systematic Basis Sets and Wave Functions. *J. Chem. Phys.* **1992**, *96*, 6796–6806.
- (55) Lynch, B. J.; Zhao, Y.; Truhlar, D. G. Effectiveness of Diffuse Basis Functions for Calculating Relative Energies by Density Functional Theory. *J. Phys. Chem. A* **2003**, *107*, 1384–1388.
- (56) Dunning, T. H., Jr. Gaussian Basis Sets for Use in Correlated Molecular Calculations. I. The Atoms Boron through Neon and Hydrogen. *J. Chem. Phys.* **1989**, *90*, 1007–1023.
- (57) *OriginPro* Version 8.6 64Bit, Data Analysis and Graphing Software; OriginLab Corporation: One Roundhouse Plaza, Northampton, MA 01060; www.OriginLab.com.
- (58) Putz, H.; Brandenburg, K. *Diamond: Crystal and Molecular Structure Visualization Crystal Impact*; Kreuzherrenstrasse 102, D-53227 Bonn, Germany; <http://www.crystalimpact.com/diamond>.
- (59) Mura, M. E.; Knowles, P. J. Improved Radial Grids for Quadrature in Molecular Density-Functional Calculations. *J. Chem. Phys.* **1996**, *104*, 9848–9858.
- (60) Becke, A. D. Density-Functional Thermochemistry. III. The Role of Exact Exchange. *J. Chem. Phys.* **1993**, *98*, 5648–5652. Becke, A. D. A New Mixing of Hartree-Fock and Local Density-Functional Theories. *J. Chem. Phys.* **1993**, *98*, 1372–1377.
- (61) Lee, C.; Yang, W.; Parr, R. G. Development of the Colle-Salvetti Correlation-Energy Formula into a Functional of the Electron Density. *Phys. Rev. B* **1988**, *37*, 785–789.
- (62) Stephens, P. J.; Devlin, F. J.; Chabalowski, C. F.; Frisch, M. J. Ab Initio Calculation of Vibrational Absorption and Circular Dichroism Spectra Using Density Functional Force Fields. *J. Phys. Chem.* **1994**, *98*, 11623–11627.
- (63) Lee, H.; Lee, C.; Parr, R. G. Conjoint Gradient Correction to the Hartree-Fock Kinetic- and Exchange-Energy Density Functionals. *Phys. Rev. A* **1991**, *44*, 768–771.

(64) Pavanello, M.; Neugebauer, J. Modelling Charge Transfer Reactions with the Frozen Density Embedding Formalism. *J. Chem. Phys.* **2011**, *135*, 234103/1–13.